Mon. Not. R. Astron. Soc. **348,** 1301–1320 (2004) doi:10.1111/j.1365-2966.2004.07445.x

Multisite observations of SU Aurigae

Y. C. Unruh,[1⋆] J.-F. Donati,[2] J. M. Oliveira,[3,4] A. Collier Cameron,[5] C. Catala,[2] H. F. Henrichs,[6] C. M. Johns-Krull,[7] B. Foing,[3] J. Hao,[8] H. Cao,[8] J. D. Landstreet,[9] H. C. Stempels,[10] J. A. de Jong,[11] J. Telting,[12] N. Walton,[13] P. Ehrenfreund,[11] A. P. Hatzes,[14,15] J. E. Neff,[16] T. Böhm,[2] T. Simon,[17] L. Kaper,[6] K. G. Strassmeier[18] and Th. Granzer[18]

[1]*Astrophysics Group, Blackett Laboratory, Imperial College of Science, Technology and Medicine, London SW7 2BW*
[2]*Laboratoire d'Astrophysique de l'Observatoire Midi-Pyrénées, Toulouse, France*
[3]*Space Science Division, ESTEC/ESA, Nordwijk, the Netherlands*
[4]*School of Chemistry and Physics, Keele University,Staffordshire ST5 5BG*
[5]*School of Physics and Astronomy, University of St Andrews, Fife KY16 9SS*
[6]*Astronomical Institute 'Anton Pannekoek', University of Amsterdam, the Netherlands*
[7]*Department of Physics and Astronomy, Rice University, Houston, TX 77005, USA*
[8]*Chinese Academy of Sciences, Beijing Astronomical Observatory, China*
[9]*Department of Physics and Astronomy, University of Western Ontario, London,Ontario N6A 3K7, Canada*
[10]*Department of Astronomy and Space Physics, Box 515, SE-75120 Uppsala, Sweden*
[11]*Leiden Observatory, PO Box 9513, 2300 RA Leiden, the Netherlands*
[12]*Nordic Optical Telescope, Apartado 474, 38700 Santa Cruz de La Palma, Spain*
[13]*Institute of Astronomy, University of Cambridge, Madingley Road, Cambridge CB3 0HA*
[14]*Department of Astronomy, The University of Texas at Austin, Austin, TX 78712, USA*
[15]*Thüringer Landessternwarte Tautenburg, Karl-Schwarzschild-Observatorium,D-07778 Tautenburg, Germany*
[16]*Department of Physics and Astronomy, College of Charleston, Charleston, SC 29424, USA*
[17]*Institute for Astronomy, University of Hawaii, 2680 Woodlawn Drive, Honolulu,HI 96822, USA*
[18]*Astrophysikalisches Institut Potsdam, An der Sternwarte 16, 14482 Potsdam, Germany*

Accepted 2003 November 19. Received 2003 November 15; in original form 2003 April 7

ABSTRACT

We present results from the 1996 Multi-Site Continuous Spectroscopy (MUSICOS) campaign on the T Tauri star SU Aurigae. We find a 2.7-d periodicity in the He I (587.6 nm) line, and somewhat longer, less well-pronounced periodicities in the Balmer lines and in Na D. Our observations support the suggestion that the wind and infall signatures are out of phase on SU Aur. We present Doppler images of SU Aur that have been obtained from least-squares deconvolved profiles. Images taken about one rotation apart show only limited overlap, in particular at low latitudes. This is due in part to limitations in signal-to-noise ratio, and in part to line-profile deformations that arise from short-lived and/or non-surface features. The agreement at high latitudes is better and suggests that at least some longer-lived features are present. The analysis of Stokes *V* profiles yields a marginal magnetic field detection during one of the phases.

Key words: stars: imaging – stars: individual: SU Aur – stars: magnetic fields – stars: pre-main-sequence.

1 INTRODUCTION

1.1 T Tauri stars

One of the outstanding problems in the study of the later stages of star formation is the nature of the mechanism by which protostars lose angular momentum as they contract. T Tauri stars (TTS) are a good test-bed for various accretion theories, in particular classical TTS, which show strong accretion signatures.

TTS are usually subdivided into three groups. The first group, classical TTS (CTTS), comprises very active pre-main-sequence stars of about 1 $M_{\odot}$ or less. Their spectra are typically characterized by excess ultraviolet (UV) and infrared (IR) emission as well as strong, low-ionization emission-line activity. This is superimposed

⋆E-mail: y.unruh@imperial.ac.uk

on to a nearly 'normal' late-type stellar absorption spectrum that is thereby diluted. This dilution can be so strong that virtually no absorption lines are visible in the most extreme CTTS. Most CTTS spectra can be explained by a model in which viscous accretion (at a rate of 10^{-8} to 10^{-6} $M_\odot$ yr^{-1}) from dusty circumstellar discs with radii of tens to hundreds of astronomical units (au) (Beichman et al. 1986; Myers et al. 1987) drives the emission-line activity (Kenyon & Hartmann 1987; Cohen, Emerson & Beichman 1989). The way the star and its disc interact, however, is still somewhat controversial. CTTS usually show very strong and erratic light-curve variations, with no clear periodicities. They are typically rather slowly rotating with rotation periods of about 5–10 d or so and may possess hotspots due to accretion shocks as well as cool starspots.

The second group is called weak-line TTS (WTTS). They are not accreting and show no evidence for a circumstellar disc (in the visible wavebands). WTTS often display higher rotation rates than their more active counterparts, with $P_{\rm rot}$ being of the order of 1–3 d [though see also Stassun et al. (1999), who found no significant difference between WTTS and CTTS rotation periods for stars in the Orion nebula]. Most WTTS have light curves that show clear periodicities and can be explained by invoking cool starspots. WTTS that show no disc signatures in the infrared are sometimes also called 'naked' T Tauri stars.

The third group consists of early-type TTS (ETTS), sometimes also called UXORs (after the prototype UX Ori). These are stars of spectral type K0 or earlier (Eaton & Herbst 1995). Strictly speaking, the ETTS objects include TTS as well as Herbig Ae/Be stars. Their light curves are characterized by strong and erratic dimmings (quite often by about 1 mag and more in the V band). The most common explanation for these dimmings is the obscuration of the stellar disc by optically thick circumstellar gas (see e.g. Grinin & Tambovtseva 1995). The presence of optically thick circumstellar discs around ETTS, however, has not yet been well established. A number of ETTS show infall signatures, usually in the form of transient redshifted absorption lines. This has prompted speculation that the infalling gas is due to evaporating solid bodies (e.g. Grinin et al. 1994; Grady et al. 1996). ETTS do not appear to show any changes in the veiling continuum.

To date, only very few T Tauri stars have been Doppler imaged. The most popular targets have been the two WTTS, V410 Tau (Joncour 1992; Joncour, Bertout & Ménard 1994a; Strassmeier 1994; Hatzes 1994; Rice & Strassmeier 1996) and HDE 283572 (Joncour, Bertout & Bouvier 1994b; Strassmeier & Rice 1998). The two more active TTS that have been imaged are DF Tau (Unruh et al. 1998) and SU Aur (Petrov et al. 1996).

Much effort has been invested recently in measuring the magnetic fields on TTS, mostly using Zeeman line broadening. Typical magnetic field measurements yield of the order of 1–2 kG for WTTS (see e.g. Basri, Marcy & Valenti 1992; Guenther & Emerson 1996). For CTTS, Johns-Krull, Valenti & Koresko (1999b) determined a mean surface magnetic field strength of 2.6 ± 0.3 kG for BP Tau, and Guenther et al. (1999) found mean magnetic fields of 2.35 ± 0.15 and 1.1 ± 0.2 kG for T Tau and Lk Ca 15 respectively. These field strengths are within the range of values needed for magnetic accretion models [though see Safier (1998) for a critique of the magnetospheric infall model]. Using spectropolarimetry, magnetic fields can be detected directly by their Zeeman signatures (in this case, no accurate spectral line synthesis is necessary). Using this technique, Donati et al. (1997) detected complex magnetic fields on the surfaces of the WTTS, V410 Tau and HD 283572. Johns-Krull et al. (1999a) found the He I (587.6 nm) emission line of BP Tau to be circularly polarized and inferred magnetic field strengths of about 2.5 kG.

Table 1. Parameters of SU Aur.

Parameter		Ref.
Spectral type	G 2	Cohen & Kuhi (1979)
Brightness (V)	9 mag	Cohen & Kuhi (1979)
Mass	2.25 $M_\odot$	Cohen & Kuhi (1979)
	1.9 $M_\odot$	Dewarf et al. (1998)
$v \sin i$	≈60 km s^{-1}	Johns-krull (1996), this paper
		this paper
Period (photom.)	1.55, 2.73 d	Herbst et al. (1987)
	⩽3.5 d	Bouvier et al. (1993)
Period (Hα wing)	≈3 d	Johns & Basri (1995b)
Period ($v_{\rm rad}$)	3.03 ± 0.03 d	Petrov et al. (1996)
Period	2.7 ± 0.3 d	his paper

1.2 SU Aur

SU Aur is a relatively bright T Tauri star that has been variously classified as a classical T Tauri star (see e.g. Giampapa et al. 1993), or early-type T Tauri star (Herbst et al. 1994). It has also been used as a prototype to define an SU Aur class of T Tauri stars (Herbig & Bell 1988). Some of its parameters are listed in Table 1. According to Akeson et al. (2002), SU Aur has a rather low disc mass of $\log(M_{\rm D}/{\rm M}_\odot) = -5.1^{+1.4}_{-0.8}$. This is considerably lower than typical classical TTS disc masses.

On account of its relative brightness, SU Aur has been the subject of several detailed spectroscopic studies (Giampapa et al. 1993; Johns & Basri 1995b; Petrov et al. 1996). Johns & Basri (1995b) put forward a magnetospheric accretion model derived from the currently favoured model for CTTS. In the CTTS accretion model, the disc is disrupted by the magnetic field of the star and accreting matter is channelled on to the star along magnetic field lines (Königl 1991; Cameron & Campbell 1993; Shu et al. 1994; Armitage & Clarke 1996). In the case of SU Aur, Johns & Basri (1995b) suggest that the magnetic dipole is slightly inclined with respect to the rotation axis of the star. Material from the disc accretes along magnetic field lines, but, because of the inclination of the dipole, accretion is seen preferentially for one half of the stellar rotation, whereas a wind is observed during the other half. This model has been dubbed the 'eggbeater'.

Even though SU Aur has been monitored frequently, the photometric period determinations are very uncertain. This is because the light curve of SU Aur does not show any clear periodic variations (see also Section 2.3). To date, the most conclusive period determinations have not come from photometric measurements, but were derived from spectral variations in the emission lines (see Johns & Basri 1995b; Petrov et al. 1996, and Table 1). In fact, most of our current knowledge stems from time-series investigations of the Balmer profiles, though, so far, observations have always suffered from relatively large phase gaps.

Despite the uncertainties in its period, SU Aur is, compared to most other classical and early-type TTS, a promising candidate for surface mapping by virtue of its small veiling and high rotation velocity. In this paper we present the observations of SU Aur taken during the 1996 MUSICOS campaign and give an overview of the emission-line and photospheric line-profile variability. In Oliveira et al. (2000a) the emission and upper-atmospheric lines were analysed in more detail.

2 OBSERVATIONS AND DATA REDUCTION

2.1 MUSICOS

The Multi-Site Continuous Spectroscopy (MUSICOS) network was set up to investigate the time-dependent behaviour of stars with rotation periods that necessitate coordinated observations from several longitudes (Catala et al. 1993).

SU Aur was chosen as one of the targets for the MUSICOS 1996 campaign that took place in November of that year. A total of 126 echelle spectra were taken over 10 nights at five different sites. At the Beijing Astronomical Observatory (BAO) in Xinglong, China, the setup consisted of a 2.2-m telescope with an echelle spectrograph and a 1024 × 1024 Tektronix detector. The 1.9-m telescope at the Observatoire de Haute Provence (OHP, France) was used with the Elodie spectrograph (Baranne et al. 1996). On the 2.1-m Isaac Newton Telescope (INT) at La Palma, Spain, the ESA MUSICOS spectrograph (Baudrand & Böhm 1992) was linked to the Cassegrain focus with a fibre-optic cable. At McDonald Observatory (MDO, Texas), we used the 2.1-m Otto Struve Telescope with the Sandiford Cassegrain echelle spectrometer (McCarthy et al. 1993). The observations at the Canada–France–Hawaii Telescope (CFHT) included observations in Stokes *V*. They were taken through a Cassegrain polarimetric unit, fibre-linked to the MUSICOS echelle spectrograph (Donati et al. 1999). The wavelength coverage and resolution of each telescope/spectrograph combination are shown in Table 2 (see also Catala et al. 1999).

Table 2. List of the observatories with the wavelength coverage and resolution of the spectrographs used.

Observatory	Detector	λλ (nm)	Resolving power
BAO (2.2 m)	1024^2 Tektronix	557–850	45 000
OHP (1.9 m)	1024^2 Tektronix	389–682	45 000
INT (2.5 m)	1024^2 Tektronix	486–849	35 000
MDO (2.1 m)	1200 × 400 Reticon	547–673	55 000
CFHT (3.5 m)	2046^2 STIS2	410–814	35 000

Table 3. Journal of observations of SU Aur from BAO in Xinglong, China. The columns in this and subsequent tables list the identifier for the observatory, the day (in 1996 November) on which the spectra were taken, the UT mid-time, modified Julian date (HJD – 245 0400), the exposure time and the number of spectra taken per group. The last column lists the approximate signal-to-noise ratio per pixel in the Hα order for a single exposure. In order to obtain an estimate of S/N per resolution element, these numbers have to be multiplied by about 1.3.

Obs.	Date	UT	MHJD	Exp. time (s)	Group size	S/N near Hα
BAO	19	15:20	7.14	1800	2	80
BAO	19	18:09	7.26	1800	1	80
BAO	19	19:52	7.33	1800	1	85
BAO	20	14:25	8.10	1800	1	50
BAO	21	13:37	9.07	1800	1	50
BAO	21	15:02	9.13	3600	1	75
BAO	21	18:27	9.27	1800	1	55
BAO	21	19:39	9.32	1800	2	60
BAO	24	13:28	12.06	1800	1	80
BAO	24	14:36	12.11	1800	2	80
BAO	24	17:58	12.25	1800	2	75
BAO	24	21:27	12.39	1800	3	50

The journals of observations are given for each observatory individually in Tables 3 to 7. The exposure time listed is the time of each individual exposure, rather than that of the complete group. Similarly, the signal-to-noise ratios listed are average ratios per pixel for a single exposure in a group. The signal-to-noise ratio per resolution element is obtained after multiplication with the factor given in the heading of each table.

The weather during the run was patchy, particularly at the CFHT, but we obtained good phase coverage between HJD 245 0406.5 and 245 0410.0, and reasonable phase coverage for the subsequent days up to HJD 245 0414.0 (see Fig. 1).

2.2 Spectroscopic data reduction

The data were reduced following standard procedures. After bias subtraction, each exposure was flat-fielded. For the data taken at the INT, BAO and MDO, the orders were extracted using the optimal extraction algorithm (Horne 1986) as implemented in ECHOMOP (Mills 1994), an echelle data reduction package distributed by Starlink. As a result of internal reflections in the MDO spectrograph, we had to

Table 4. Journal of observations for SU Aur from the OHP, France (columns as per Table 3). In order to obtain an estimate of S/N per resolution element in the Hα order, the numbers listed in the last column have to be multiplied by 1.5.

Obs.	Date	UT	MHJD	Exp. time (s)	Group size	S/N near Hα
OHP	18	22:14	6.43	1800	3	25
OHP	19	03:22	6.64	1800	3	35
OHP	20	21:55	8.41	1800	3	40
OHP	21	01:32	8.56	1800	3	55
OHP	21	04:24	8.68	1800	2	50
OHP	23	22:12	11.43	1800	3	45
OHP	24	01:32	11.56	1800	2	50
OHP	24	05:00	11.71	1800	2	30
OHP	24	21:31	12.40	1800	2	50

Table 5. Journal of observations for SU Aur from the INT, La Palma (columns as per Table 3). The multiplication factor to obtain S/N for each resolution element is 1.4.

Obs.	Date	UT	MHJD	Exp. time (s)	Group size	S/N near Hα
INT	17	02:08	4.59	1200	1	60
INT	19	23:05	7.46	1800	2	55
INT	20	03:56	7.66	1800	2	60
INT	20	05:55	7.79	1800	2	70
INT	20	22:40	8.44	1800	2	60
INT	21	01:09	8.55	1800	2	55
INT	21	03:25	8.64	1800	2	75
INT	21	05:39	8.74	1800	1	85
INT	21	23:18	9.47	1800	2	65
INT	22	01:27	9.56	1800	2	65
INT	22	03:35	9.65	1800	2	60
INT	22	06:10	9.76	1800	2	60
INT	23	23:14	11.47	1800	2	40
INT	24	01:08	11.55	1800	1	60
INT	24	01:47	11.57	900	2	40
INT	24	03:49	11.66	670	1	35
INT	24	21:50	12.41	1200	3	45
INT	25	00:20	12.51	1200	3	60
INT	25	03:26	12.64	1200	3	65
INT	25	22:14	13.43	900	2	35

Table 6. Journal of observations for SU Aur from the McDonald Observatory, Texas (columns as per Table 3). The multiplication factor for S/N is 1.4.

Obs.	Date	UT	MHJD	Exp. time (s)	Group size	S/N near Hα
MDO	19	05:36	6.73	1800	1	110
MDO	19	06:03	6.75	1200	1	95
MDO	19	08:05	6.84	1300	2	105
MDO	19	10:33	6.94	1500	2	115
MDO	19	12:14	7.01	1500	1	100
MDO	20	06:05	7.75	1500	2	95
MDO	20	08:38	7.86	1600	1	80
MDO	20	09:10	7.88	1800	1	80
MDO	20	12:02	8.00	1800	2	85
MDO	21	06:20	8.76	1800	2	95
MDO	21	09:04	8.88	1600	2	115
MDO	21	11:15	8.97	1600	1	90
MDO	21	11:46	8.99	1800	1	80
MDO	22	05:36	9.73	1600	1	80
MDO	22	07:42	9.82	1500	2	100
MDO	22	10:17	9.93	1800	2	100
MDO	23	05:33	10.73	1800	2	85
MDO	23	08:34	10.86	1800	1	110
MDO	23	09:03	10.88	1600	1	110
MDO	25	05:24	12.73	1800	2	80
MDO	25	08:08	12.84	1800	2	80
MDO	25	10:39	12.94	1800	2	80
MDO	26	04:14	13.68	1800	1	85

Table 7. Journal of observations for SU Aur from the Canada–France–Hawaii Telescope (columns as per Table 3). The multiplication factor for S/N is 1.5.

Obs.	Date	UT	MHJD	Exp. time (s)	Group size	S/N near Hα
CFHT	19	09:39	6.90	600	4	55
CFHT	19	12:40	7.03	600	4	50
CFHT	20	08:14	7.84	600	4	60
CFHT	21	14:18	9.10	600	4	30
CFHT	26	08:55	13.87	600	4	30
CFHT	26	11:30	13.98	600	4	50
CFHT	27	10:35	14.94	600	4	50
CFHT	27	11:34	14.98	600	4	45
CFHT	27	14:37	15.11	600	4	35

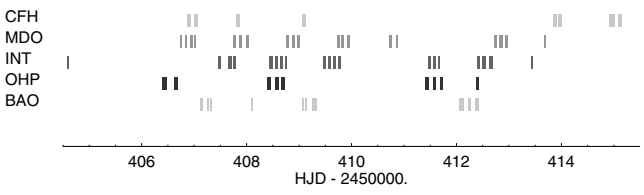

Figure 1. Phase coverage during the MUSICOS campaign.

reject two orders in the 610 nm wavelength region. In the case of the OHP, the data are automatically reduced at the observatory with the INTER-TACOS procedure (Baranne et al. 1996) and were used as such.

The reduction of the polarimetric data from the CFHT was performed using a dedicated procedure for extracting Stokes V and I parameters developed as part of the 'ESPRIT' data reduction package by Donati et al. (1997). Each exposure is a combination of four subexposures that have to be taken in order to get rid of background and instrumental polarization. The data reduction is described in detail in Donati et al. (1997).

We have not attempted to flux-calibrate our spectra, as this is notoriously difficult for echelle observations without simultaneous low-resolution spectroscopy or photometry. When we refer to 'flux' we are therefore not considering absolute flux values but the flux above (or below) the normalized continuum. Finally, as the resolution is different for each telescope, we have rebinned all the single-line spectra shown here to a uniform resolution of $\lambda/\Delta\lambda = 30\,000$, corresponding to a velocity resolution of about 10 km s^{-1}. The convolved profiles used for the Doppler imaging in Section 4.3 are binned to a resolution of $\lambda/\Delta\lambda = 40\,000$.

2.3 Photometry

Unfortunately, there is no contemporaneous light curve with good phase coverage. SU Aur was monitored during the 1996/1997 observing season with the Automatic Photometric Telescope (APT) of the University of Vienna (Strassmeier et al. 1997; Strassmeier, Serkowitsch & Granzer 1999), but only a few data points could be secured during the spectroscopic campaign. The light curve is shown in Fig. 2. Typically for SU Aur, we can detect no clear rotational modulation in the light curve. Instead, it shows strong and erratic dimmings during which the star gets fainter by typically about 0.5 mag in the V band within 3–5 d. The recovery is usually slower and can take 10 d or so [see Dewarf, Guinan & Shaughnessy (1998) and Nadalin, Dewarf & Guinan (2000) for a description of similar events]. This behaviour is typical for SU Aur and prompted Herbst et al. (1994) to classify SU Aur as an ETTS (UXOR) variable. SU Aur's dimmings are not quite as dramatic as those of other ETTS, which easily exceed differences of one magnitude in the V band.

One such dimming event was observed starting from about HJD 245 0408.5 during our spectroscopic monitoring campaign when the star's V-band magnitude decreased by more than 0.5 over the course of about 3 d. Unfortunately, the weather at the APT was such that only one night between HJD 245 0410 and 245 0416 was clear. At HJD 245 0417, the star was again dimmer by 0.6 mag (in V) than 'usual', but as a result of our lack of data we cannot say whether it recovered between HJD 245 0410 and 245 0417. In agreement with what has been observed for other ETTS, SU Aur becomes redder as it gets fainter (see lower right-hand plot in Fig. 2). However, during the 1996/1997 observing season, it does not show the 'colour reversal' typical for ETTS, where the stars become bluer as they enter strong brightness minima (see e.g. Eaton & Herbst 1995). This could be due to the fact that the dimmings that we observed were not very extreme. As it is the disc that is believed to be responsible for the bluer colours of the systems once the star itself has been sufficiently occulted, the lack of colour reversal could also be due to SU Aur's disc being unusually faint.

3 PERIOD DETERMINATIONS

Photometric period determinations are difficult, as SU Aur's brightness varies erratically (see Fig. 2). Photometric period measurements range from as short as 1.7 d (Nadalin et al. 2000) and 1.55 d through 2.73 d (Herbst et al. 1987) up to 3.4 d (Bouvier et al. 1993). For SU Aur, spectral line-profile variations seem to offer a better chance of tracking the star's rotation, though one has to bear in mind that a line such as Hα is formed at various heights in the stellar atmosphere and under a plethora of different conditions. The identification of Balmer-line variations with the surface rotation of the star therefore remains somewhat uncertain.

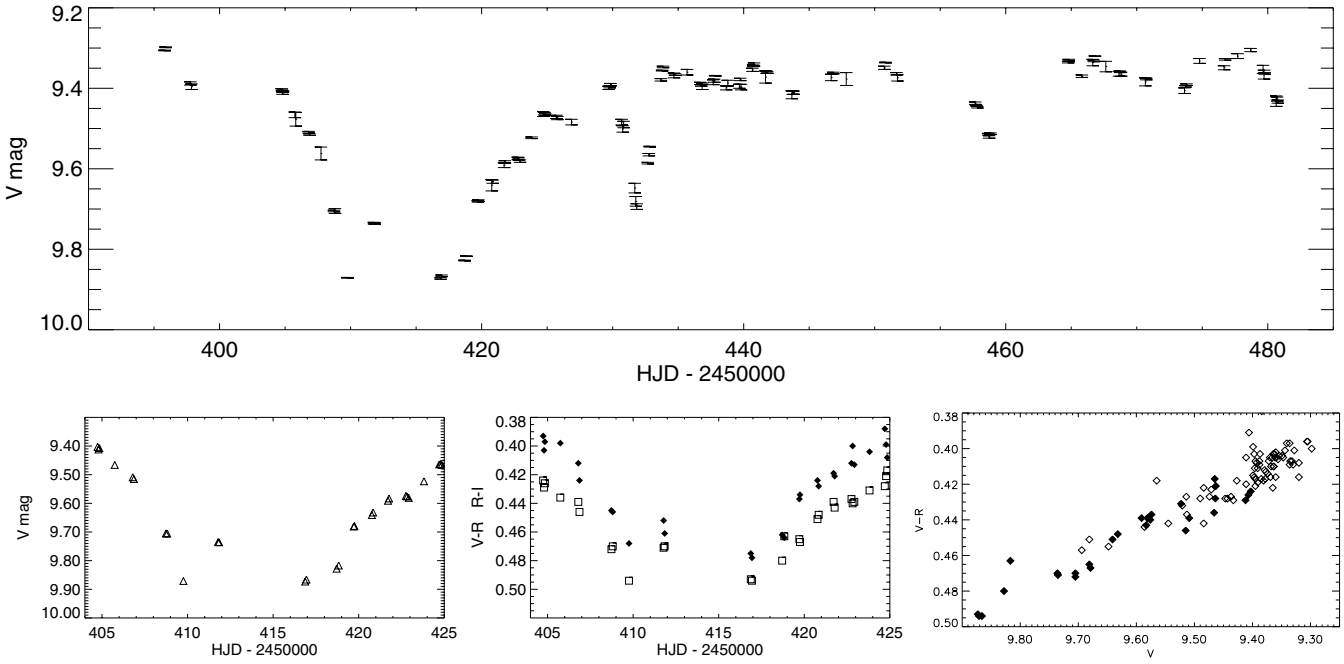

Figure 2. The photometric light curve of SU Aur taken with the University of Vienna's APT in Fairbanks, Arizona. The *x*-axes show modified HJD, i.e. HJD − 245 0000. The top graph shows the *V*-band light curve over the course of almost 90 d. The bottom left graph shows the enlarged light curve during the MUSICOS campaign, but also including the recovery phase of the obscuration event. The middle plot shows $V - R$ (lower curve, open squares) and $R - I$ (top curve, solid diamonds) during the campaign. The bottom right-hand plot shows $V - R$ versus V during the 1996/1997 observing season. The filled symbols are for data taken between HJD 245 0405 and 245 0425.

Several period measurements have been obtained from analyses of the Balmer lines and of the He D_3 line, all of them indicating periods around 3 d (Giampapa et al. 1993; Johns & Basri 1995b; Petrov et al. 1996). Johns & Basri (1995b) furthermore found that the behaviour of the red wing of Hβ and the blue wings of Hα and Hβ were anticorrelated. This was interpreted as the signature of a magnetic infall and wind, in what they called the 'eggbeater' model (see Section 1.1 and Johns & Basri 1995b), which has so far proven remarkably successful at explaining a range of accretion and wind phenomena.

The measurements referred to above were taken from single-site observations. This introduces problems, as the lifetimes of the rotationally modulated features seem to be short, perhaps due to unsteady accretion. Indeed, Smith et al. (1999) concluded that, for SU Aurigae, the dominant variability time-scale for Hα is of the order of or shorter than 1 h.

In the following we discuss the line-profile changes and associated periods for Hα, Hβ, Na D and He I (587.6 nm). Starting from 2D periodograms, we sum the fluxes in those velocity bins that show strong power peaks and use three different methods to search for periods. Note that adding the fluxes degrades the frequency resolution somewhat, though we took care to sum only velocity bands with very similar appearance on the original periodograms. The main results of our period search are presented in Table 8 and the period-search methods are outlined in the following section.

Table 8. The periods found in the normalized Lomb–Scargle periodograms (column 3), and from the flux variations using the 'clean' algorithm (column 6) and the entropy minimization technique (column 8). The second column gives the range of velocity bins that have been co-added for the periodogram. For the periods calculated using the Lomb–Scargle algorithm, we have listed the false-alarm probability (FAP) according to a Monte Carlo bootstrap method. The FAP for the 'cleaned' periods is below 10^{-5} for all periods (and has not been listed, see text). The ranges listed in columns 4 and 7 give a very conservative estimate on the period, assuming that the width of the power peak at half-maximum can be used as an indication of the possible spread in the period. For the entropy minimization, the error on the period as well as its significance are listed in columns 9 and 10. The last row shows the period for the equivalent width variations of the He I line.

Line	Velocity (km s^{-1})	P_{LS} (d)	Range (d)	FAP	P_{Cl} (d)	Range (d)	P_E (d)	Error (d)	Significance (σ)
(1)	(2)	(3)	(4)	(5)	(6)	(7)	(8)	(9)	(10)
Hα	−300... −210	2.8	2.4... 3.5	2×10^{-10}	2.9	2.4... 3.6	2.9	0.2	7
Hα	−180... −130	5.1	3.6... 8.9	5×10^{-14}	5.3	3.9... 7.7	∼6	–	–
Hα	170... 250	4.7	3.9... 6.8	2×10^{-15}	4.8	3.9... 6.2	–	–	–
Hβ	60... 185	2.7	2.2... 3.2	3×10^{-12}	2.6	2.4... 3.1	2.84	0.22	8
He I	20... 50	2.6	2.3... 3.2	2×10^{-14}	2.7	2.3... 3.1	–	–	–
He I	100... 120	2.7	2.3... 3.3	4×10^{-14}	2.7	2.3... 3.2	–	–	–
Na D	50... 70	2.6	2.3... 3.2	10^{-10}	2.7	2.3... 3.2	–	–	–
He I	–	2.7	2.3... 3.3	3×10^{-16}	2.7	2.3... 3.2	2.72	0.18	21

3.1 Period-search methods

The three methods used to search for periods are the Lomb–Scargle algorithm, the 'clean' algorithm and a technique based on the minimization of information entropy. The Lomb–Scargle algorithm is well suited to irregularly spaced data and is described in Horne & Baliunas (1986) and Press et al. (1992). When applied to the summed fluxes, the false-alarm probability (FAP), which gives an indication of the likelihood that a given power peak is due to random noise, was calculated using a Monte Carlo bootstrap method. For this we ran 1000 trials where we randomly selected fluxes from our original data set while leaving the number of data points and location (i.e. observing time) unchanged. We then calculated the periodogram for each synthetic data set, noting the maximum power for each trial. We plotted the probability for a given power value (in the power ranges obtained in the simulations) and extrapolated this to predict the probability of the actual power at the period found for the original data set. In each case the highest values of the power found for the 1000 synthetic data sets were less than half of the power peaks in the observed data.

Once a period has been determined, one obviously seeks to obtain an error estimate for this period. Most formulae for calculating the errors in the frequency (such as e.g. Horne & Baliunas 1986; Montgomery & O'Donoghue 1999) assume that the signal to be subtracted is sinusoidal. It turns out that this is not a good assumption for this data set. We therefore adopt a very conservative estimate and list the range of the periods that lie within the full width at half-maximum (FWHM) of the power peaks. The nominal error on the period is more than one order of magnitude lower than this.

The second method that we used is the 'clean' algorithm (Roberts, Lehár & Dreher 1987) as implemented in the program PERIOD (Dhillon & Privett 1997) distributed through Starlink. The periodograms are shown in Fig. 13 and the periods and their uncertainty ranges are listed in columns 6 and 7 of Table 8. The implementation of the 'clean algorithm' that we used also calculates the FAP using the bootstrap method outlined above; however, it only gives numerical values in excess of about 10^{-5}, setting all other values automatically to zero. In our case, all FAPs were nominally 'zero', i.e. below 10^{-5}, and are therefore not listed in Table 8.

Prompted by the non-sinusoidal shape of the He I (587.6 nm) equivalent-width variations (see below), we decided to explore a third method for period searches which relaxes the fundamental assumption of sinusoidal variations, namely phase dispersion minimization (e.g. Stellingwerf 1978). For our particular purposes we use the information entropy minimization technique of Cincotta, Méndez & Núñez (1995). In this scheme, several periods are tried and, for each one, the data are phased up on the given period. The data are normalized in amplitude and phase from 0 to 1. The idea is to measure how much of this normalized area is filled with data points. Random signals will fill the area with data points while periodic signals will define a curve. The degree of space filling is quantified by the information entropy and periodic signals produce a minimum in the entropy at the appropriate period. In this method, the user chooses the period range to search, the number of trial periods to explore, and the number of squares into which to divide the total normalized area (phase × amplitude).

Typically we searched periods ranging from 0.5 to 10 d at 2000 evenly spaced points and we found that nine squares produced the best results. The period uncertainty was again taken from the width of the minima and the significance of the period estimated using a Monte Carlo simulation of the data. The results from this method are listed in the last three columns of Table 8.

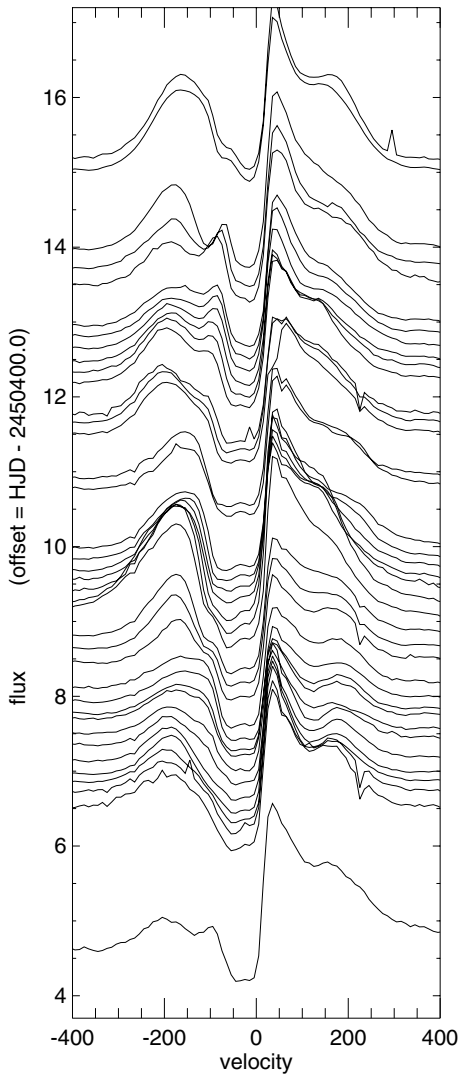

Figure 3. Stacked Hα profiles. For clarity, we have grouped together profiles that have been observed within 4 h of each other. The continuum flux has been normalized and the *y*-axis offsets of the profiles correspond to the modified HJD of the exposure times, i.e. HJD−245 0400.

3.2 Hα

SU Aur shows only Hα in emission. The higher Balmer lines are in absorption, though they show varying degrees of filling in. Hα is a relatively 'typical' wind profile with a marked blueshifted absorption component that tends to reach below the continuum. It is highly variable on a number of time-scales, as illustrated in Fig. 3. Especially notable are the redward-moving features that appear at a velocity of about -100 km s^{-1} around HJD 245 0408 and 245 0412 (see Oliveira et al. 2000 for a discussion) and the strong enhancement of the blue emission wing at approximately HJD 245 0409 when the star was at its faintest during the campaign (see Section 6).

The main plot in Fig. 4 shows the Lomb–Scargle periodogram (see Horne & Baliunas 1986; Press et al. 1992) for Hα. The false-alarm probability (FAP) has been calculated for each velocity bin according to Press et al. (1992). The FAP gives an estimate of how likely it is that a peak of a given height is due to random noise, a low value indicating a significant signal. The FAP is below 10^{-6} for all contours drawn in Fig. 4. We note that the formula given by Press

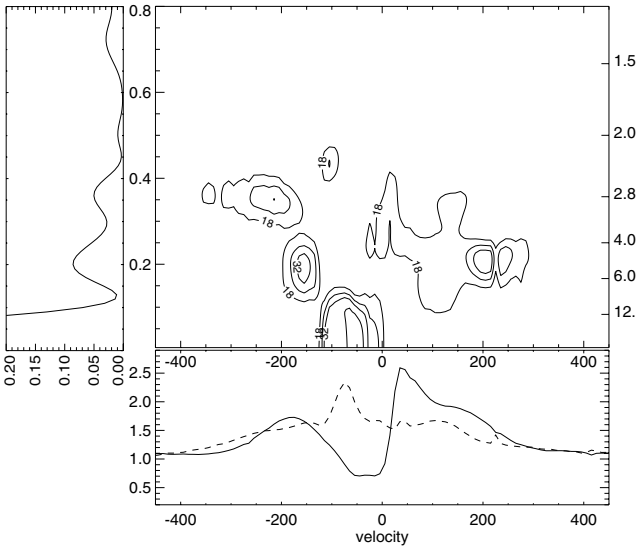

Figure 4. Main plot: The normalized Lomb–Scargle periodogram of the Hα profiles of SU Aur. The left-hand axis shows the frequency (d^{-1}), and the right-hand axis the period (d). The contours are normalized powers of 18, 26, 32 and 40. The lowest contours correspond to a false-alarm probability (FAP) of about 10^{-6}. To the left of the periodogram, we have plotted the window function for Hα. It has been scaled so that the power at zero frequency is unity. Underneath the periodogram the normalized mean (solid line) and variance profile (dashed line) are shown. The normalized variance profile has been multiplied by a factor of 4 and offset by 1. It was calculated according to $[\sum(f_i - \bar{f})^2/(n-1)]^{0.5}/\bar{f}$ Johns & Basri 1995a), where $\bar{f}$ is the mean profile.

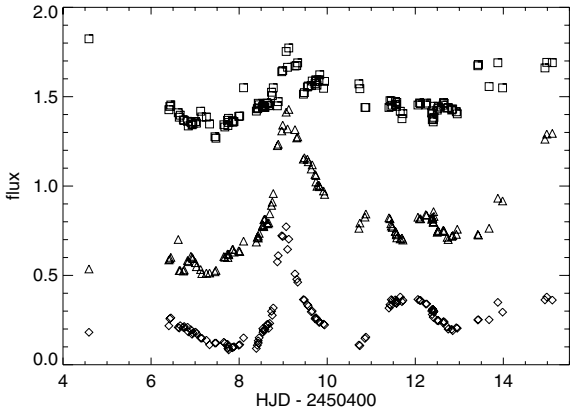

Figure 5. The flux in Hα above the (normalized) continuum in three different velocity bins. The diamonds show the flux variations in the blue emission peak where the 3-d period was found (-300 to -210 km s^{-1}. The triangles show the variations of a bin spanning -180 to -130 km s^{-1}, where the periodogram suggests a 5-d period. The squares show the flux variations in the red wing, where the periodogram also suggests a 5-d period (170 to 250 km s^{-1}). For clarity, the triangles and diamonds have been offset by -0.7 and -1.0 respectively.

et al. (1992) can underestimate the FAP considerably, in particular when the data points show strong clumping. A more accurate method to estimate the FAP is to run a bootstrap Monte Carlo simulation, as we have done for selected velocity bins (see Table 8).

Along the frequency axis of each periodogram we have plotted the window function (as obtained from a discrete Fourier transform, since it is not possible to use the Lomb–Scargle analysis for windowed data). Underneath the periodogram we have sketched the mean profile (solid line) and the normalized variance profile (dashed line). Two periodicities at around 3 d and 5 d are apparent for Hα. The one at approximately 3 d is that previously identified by Johns & Basri (1995b) and Petrov et al. (1996). While Johns & Basri (1995b) found the 3-d period in a velocity bin ranging from about -250 to -100 km s^{-1}, we find a period of approximately 3 d further towards the blue, in a range from -300 to -170 km s^{-1}. This 3-d period seems to be due to a weakening and strengthening of the outer blue wing. At the same time, we find a 5-d periodicity centred around a velocity of -150 km s^{-1} [where Johns & Basri (1995b) found the strongest evidence for a 3-d period] and over almost all of the red emission wing.

We suggest that the 5-d period is spurious, as the shape of the window function allows for substantial leakage into the 5-d bin (see Fig. 4). Furthermore, we do not find much evidence for a 5-d period when the intensities of the Hα profile are plotted against time in the regions where periodicities are suggested in the periodogram (see Fig. 5). We found that exclusion of the profiles between HJD 245 0409 and 245 0410, which show the strong flux enhancement, leaves the position of the power peaks largely intact, so that it is unlikely that the flux enhancement alone is responsible for the 5-d period.

3.3 Hβ

Because of its different source function, Hβ is formed over a smaller range of temperatures and densities than Hα. Theoretical studies (see e.g. Calvet & Hartmann 1992; Hartmann, Hewett & Calvet 1994) as well as observations (Edwards et al. 1994) have shown that Hβ reveals the signature of mass infall much more readily than Hα. This is indeed also the case for SU Aur.

Fig. 6 shows the stacked and grouped profiles of Hβ during our run, where we have subtracted the rotationally broadened Hβ profile of the Sun. We were able to observe Hβ simultaneously from only three of the sites (CFHT, INT and OHP) and therefore obtained rather poor phase coverage. The periodogram for Hβ is shown in Fig. 7. In agreement with Johns & Basri (1995b), we find that the period of approximately 3 d now occurs in the red as well as in the blue part of the profile. The periodicity in the red wing is not only apparent in the periodogram, but is, in contrast to Hα, now also visible in the stacked spectra (Fig. 6). As already suggested by the lower and less well-defined peaks in the periodogram, the periodicity in the blue wing is harder to trace.

Johns & Basri (1995b) suggested that the red and blue wings of the Hβ line are anticorrelated. Because of a lack of phase coverage and the presence of the small moving emission bumps in the blue profile wings, it is hard to see this directly in Fig. 6, though more detailed analysis essentially confirms their original conjecture. We refer to Oliveira et al. (2000) for plots showing the anticorrelation between the red and blue wings.

3.4 Na D doublet

Owing to the interstellar absorption lines, light pollution and lower intrinsic variability, the sodium doublet is slightly more difficult to analyse. However, it still shows a number of similarities with the Balmer lines, including redward-moving features in the blue absorption wings (see Oliveira et al. 2000, for a detailed analysis). The periodogram for the Na D lines is shown in Fig. 8. We recover once again a period of slightly less than 3 d in the red parts (from about 30 to 130 km s^{-1}) of the profile. In the same velocity region,

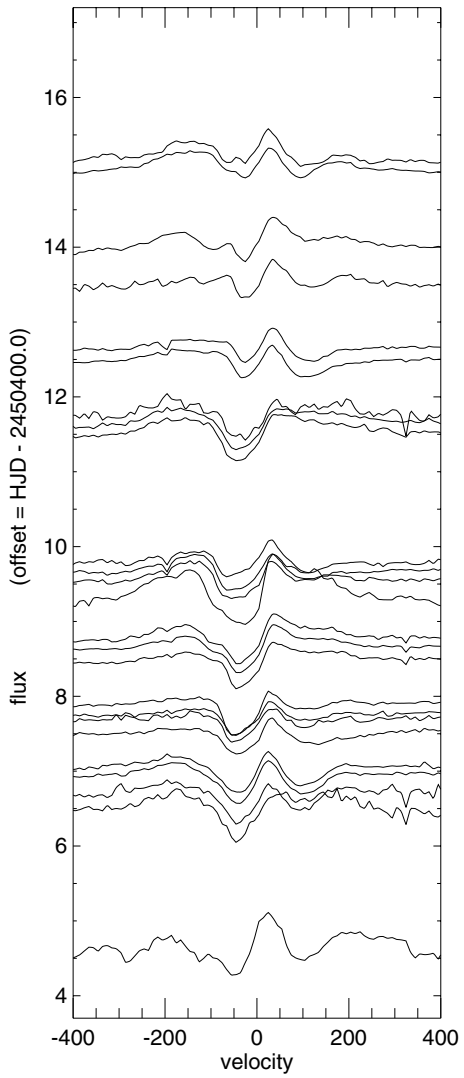

Figure 6. Stacked Hβ profiles. For clarity, we have grouped together profiles in 4-h bins. The continuum flux has been normalized and the *y*-axis offsets of the profiles correspond to the observing times (HJD−245 0400). The broadened profile of the Sun has been subtracted from all spectra.

we can now also see a strong secondary period at about 1.4 d. The variability at the line centre is strong, but does not show any periodicities. As with Hα, there is also a (probably spurious) power peak close to 5 d, though now only in a narrow velocity range centred at -70 km s^{-1}.

3.5 He I 587.6 nm

The stacked profiles of the He I 587.6 nm line are shown in Fig. 9. This plot clearly shows the dramatic changes in linestrength and the mostly asymmetric shape of the line profile. Oliveira et al. (2000) argued that the He line can most easily be understood in terms of a superposition of two absorption components, one at rest velocity, and one redshifted by about 80 km s^{-1}. Note that, while the minimum observed He equivalent width of about 50 mÅ is not too dissimilar to what is usually observed on G dwarfs (Saar et al. 1997), the maxima of up to 600 mÅ are quite exceptional. Solar observations show that the He D_3 absorption increases in strength with increasing activity, but then starts to fill and, for the largest flares, turns into

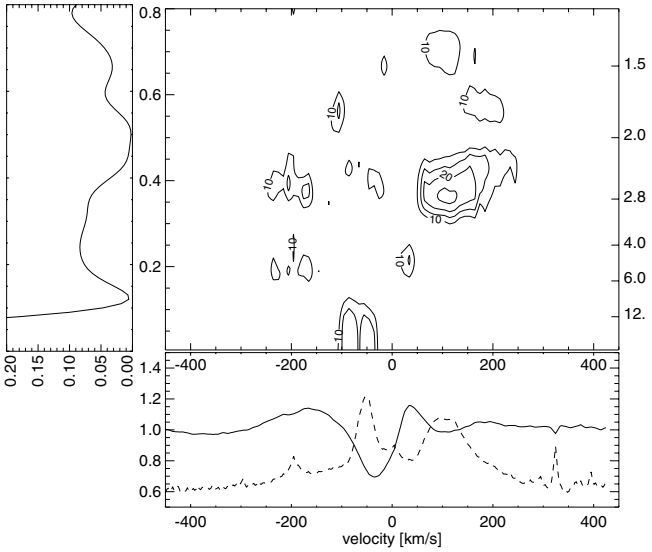

Figure 7. Main plot: The normalized Lomb–Scargle periodogram of the Hβ profiles of SU Aur. The *y*-axes show the frequency (on the left) and the period (on the right). Also shown to the left is the window function for Hβ. The FAP of the lowest contour is 2×10^{-3}, and the FAP of the second contour (at a normalized power of 15) is 10^{-6}. The bottom panel shows the Hβ mean profile (solid line) along with the variance profile (dashed line). In both cases the rotationally broadened solar Hβ profile has been subtracted. The variance profile has also been expanded by a factor of 4 and offset by 0.5.

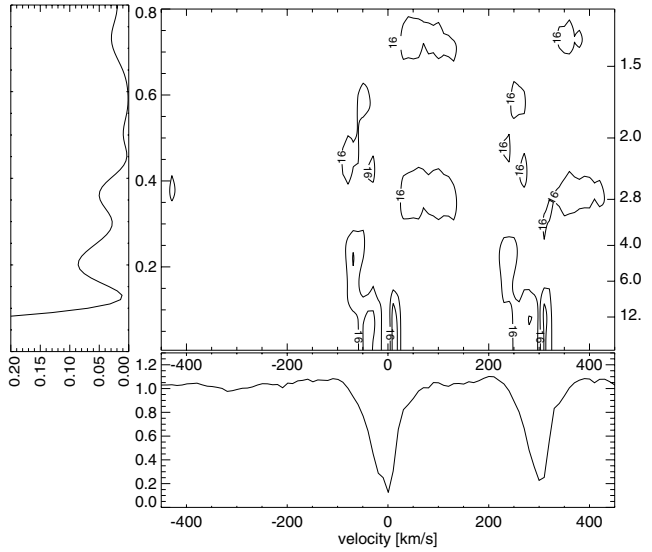

Figure 8. Main plot: The normalized Lomb–Scargle periodogram of the Na D profiles of SU Aur. The window function of the data set is shown to the left. The lowest contour corresponds to a FAP of 7×10^{-6}. The mean Na D profiles are shown in the bottom plot.

emission (Švestka 1972). Bray (1964) reports equivalent widths of up to 400 mÅ in solar flares, but more recent observations seem to have focused on large and off-limb or near-limb flares that tend to show He D_3 in emission.

In their He-line formation calculations, Andretta & Giampapa (1995) identify two distinct formation regions in dwarf atmospheres, namely in the upper chromosphere and in the much hotter plateau

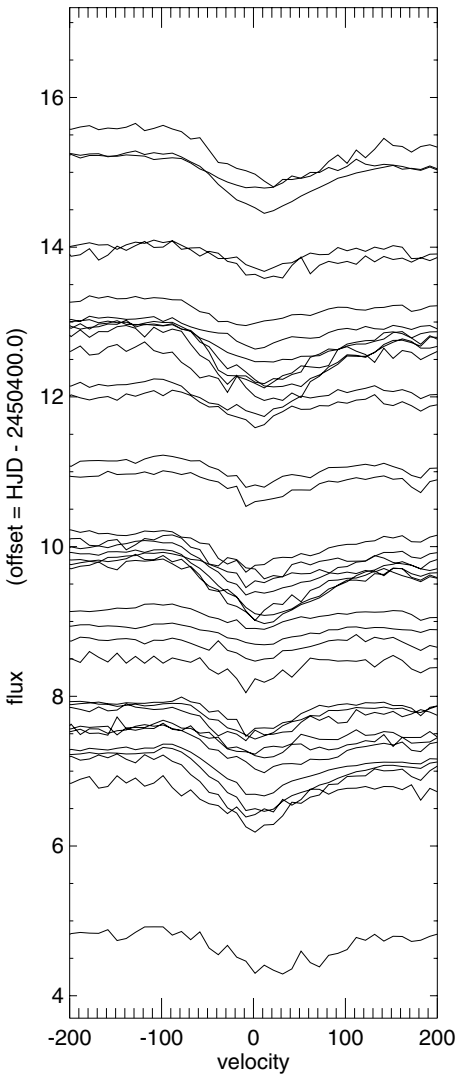

Figure 9. The stacked He I profiles, grouped together in 4-h bins. As the line-profile changes in the helium line are not very large, they have been amplified by a factor of 4 for this plot. (Despite other appearances, the noise level for the He I profiles is in fact very similar to the noise level for Na D).

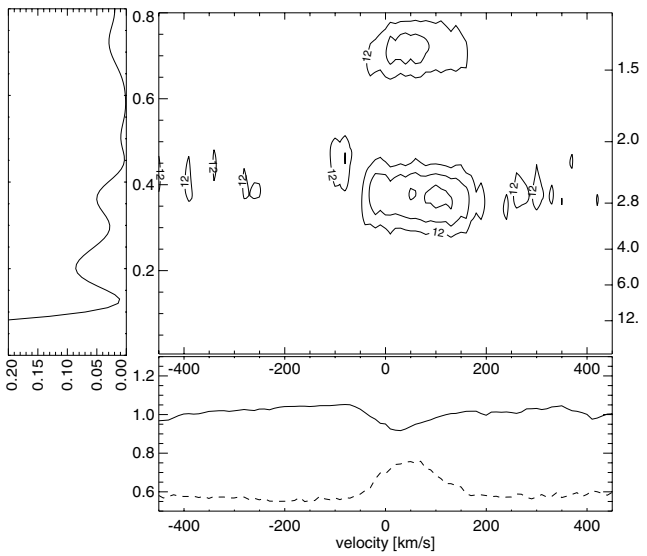

Figure 10. Main plot: The normalized Lomb–Scargle periodogram of the He I profiles of SU Aur. The window function is shown on the left. Peaks higher than the lowest contour have a FAP of less than 4×10^{-4}. Bottom: The mean and variance profile of He I over the run. The variance profile (dashed line) has been amplified by a factor of 4 and offset by 0.5.

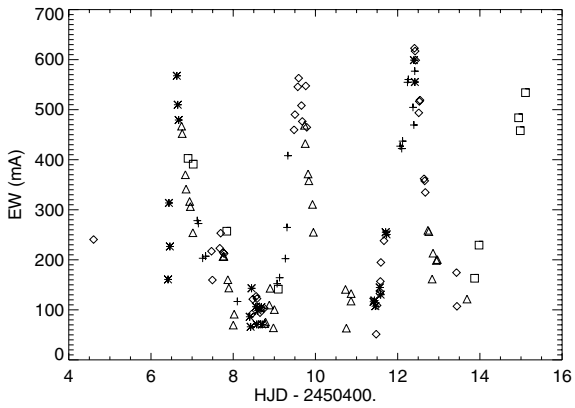

Figure 11. The He I equivalent width as a function of time. The different symbols show measurements from the different observatories, namely the BAO (plus signs), OHP (asterisks), INT (diamonds), MDO (triangles) and CFHT (squares).

region. In the density regimes considered by Andretta & Giampapa (1995), the 'turnover' where the equivalent width starts to decrease due to reversal is never reached and they estimate a maximum equivalent width of 100–150 mÅ. This is expected to increase for subgiants. Note that the strength of the He D_3 line is sensitive mainly to electron density rather than to temperature.

The 2D Lomb–Scargle periodogram for He D_3 is shown in Fig. 10. It shows a very clear periodicity at 2.7 d with a strong secondary peak at 1.4 d for velocities ranging from about -30 to 160 km s^{-1}. Petrov et al. (1996) observed periodic or quasi-periodic radial-velocity variations in the Balmer lines and in He D_3. We find that there is indeed a trend for the radial velocity to be further redshifted as the equivalent width of the He line increases. However, because of the line asymmetry, the velocity shift of the line centre is not very well determined. The periodically varying equivalent widths of the absorption, however, are readily apparent, as illustrated in Fig. 11. The variations are clearly non-sinusoidal and display very strong and sharp peaks for the largest equivalent widths. This is what first prompted us to use the phase-minimization technique, which indeed places somewhat narrower constraints on the period of the He I variations (see Table 8).

The period dependence of the entropy is plotted for the He I line in Fig. 12 and shows a very pronounced minimum at 2.7 d. The secondary period of about 1.4 d is also recovered, though it is less prominent than in the corresponding 'cleaned' or Lomb–Scargle periodograms. The dashed line shows the mean entropy for 1000 independent Monte Carlo trials. The 1000 individual trials look very similar to the mean shown in the figure. For each trial, the entropy minimum was recorded. The distribution of the 1000 trial minima peaks at an entropy of 0.8745, with a fairly sharp cut-off above this value and a Gaussian tail extending to lower entropy values. None of the trials produced a minimum lower than 0.843, while the original He I data show a minimum entropy of 0.675 at a period of 2.7 d. From a Gaussian fit to the peak and lower values of the trial

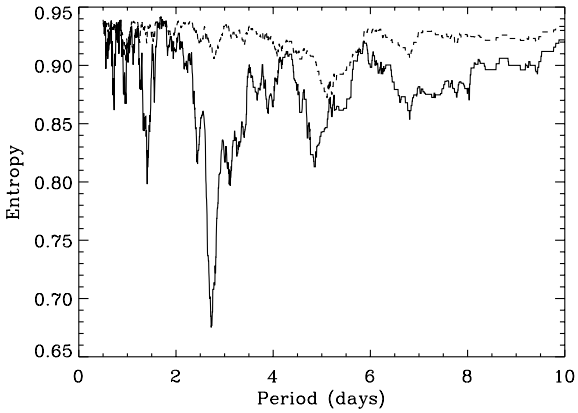

Figure 12. The solid line shows the entropy as a function of period for the He I equivalent width (see text). Also shown is the mean entropy for 1000 Monte Carlo trials where the time spacing has been kept while the order of the equivalent width data points has been randomized.

distribution, we find that the 2.7-d period is significant at the $>21\sigma$ level.

We find essentially the same periodicity in both components of the He I line, though the shape of the periodogram is somewhat different in that the variability is stronger and the secondary peak is more pronounced in the main absorption line than in the redshifted component (see Fig. 13d). Note that Oliveira et al. (2000) found that the variability of the redshifted absorption correlated well with the redshifted absorption of the Na D lines, but lagged behind that of the helium rest-velocity component.

3.6 Comparison of the different lines and methods

The results from our period searches were summarized in Table 8 and, for the 'clean' algorithm, are also plotted in Fig. 13. While there are small differences in the periods found for the different lines, with the periods recovered for the Hα line being the largest (2.8 and 2.9 d), the widths of the power peaks are such that a single period is compatible with all our observations. We favour the slightly shorter periods obtained in lines other than Hα, mainly because of the large range of regimes where Hα is formed, some of which may be well away from the stellar surface. There may hence not be sufficient magnetic 'locking' to force corotation and a single well-defined period.

The widths of the power peaks do not change noticeably when isolated measurements such as the first INT exposure or the last three CFHT exposures are excluded. We suspect that this is due to several features of our data and the star, the main ones being that we have only covered two to three rotation periods and that the variations are generally non-sinusoidal. Note that the entropy minimization technique, which does not assume sinusoidal variations, shows a much narrower peak than either the Lomb–Scargle or the 'clean' method. Furthermore, we find that the window function allows for some leakage of power at a frequency of about 0.37 d^{-1}, or a period of 2.6 d, which is uncomfortably close to our main period. Inspection of the stacked profiles also shows that, while profiles that are separated by approximately one period do show similarities in the velocity range of the power peaks, they are certainly subject to strong variations between one period and the next. We are hence dealing with a star with very strong intrinsic variability. One also has to keep in mind that the strong dimming of SU Aur may have introduced an additional trend in the fluxes. One of the characteristics of ETTS is the erratic dimming with simultaneous increases in the Hα relative flux. Unfortunately, our photometric time coverage is too sparse to allow cross-correlations between the photometric fluxes and the spectroscopic data.

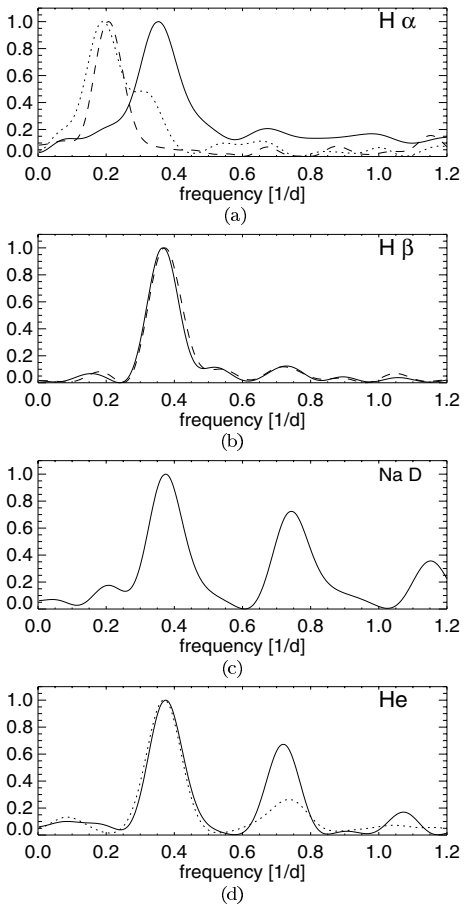

Figure 13. Top to bottom: the 'cleaned' periodograms for Hα, Hβ, Na D and He. The periodogram for Hα shows the power over several velocity ranges, namely -300 to -210 km s^{-1} (solid line), -180 to -130 km s^{-1} (dotted line) and 170 to 250 km s^{-1}(dashed line). These bins correspond to the ones chosen for the flux plots in Fig. 5 and also represent the bins with largest power in the 2D Lomb–Scargle periodogram. The Hβ periodogram is for the average flux between 60 and 185 km s^{-1}; taking a smaller bin width results in a very similar periodogram with the same main period. The Na D periodogram is for flux between 50 and 70 km s^{-1}. For He I, the solid line is for the average flux between 20 and 50 km s^{-1}, while the dashed line is for an average taken from 100 to 120 km s^{-1}.

4 PHOTOSPHERIC LINES AND DOPPLER IMAGES

4.1 Least-squares deconvolution

One of the original aims of the MUSICOS campaign was to obtain Doppler images of SU Aur and to locate possible infall sites for matter accreting from the stellar disc. The presence of spots on the stellar surface should produce line-profile deformations in the photospheric lines. However, in our case, the signal-to-noise ratio (S/N) is not good enough to allow us to detect these deformations in individual photospheric lines. One possibility is to combine the information contained in all the photospheric lines in the observed spectral range so as to increase S/N. We have done this using the

technique of least-squares deconvolution (LSD, see e.g. Donati et al. 1997; Barnes et al. 1998). As we have gathered data at five different observatories with different setups, it was not possible to use the same lines in the deconvolution for each observatory.

One implicit assumption when using LSD profiles for Doppler images is that all lines used in the deconvolution should show a similar response to surface inhomogeneities. To test this, we generated LSD profiles with different line subsets, such as e.g. singly ionized lines, 'light' elements, lines in the red or blue parts of the spectrum only, or strong lines only. This was done for the CFHT data only, as they provided a large spectral range and the best S/N.

Subsetting for different elements or ionization stages is not straightforward, as neighbouring blends can easily skew the profiles. The only element lighter than calcium that showed relatively unblended lines in our wavelength range was silicon, and we were only able to use four lines. The dashed line in the top panel of Fig. 14 shows the profile for the four silicon lines for the CFHT. The solid line is the LSD profile for all elements heavier than and including calcium. Both profiles are 'mean' profiles, where the six exposures with the highest S/N have been added. The mean silicon profile is very asymmetric, with more absorption in the red part of the line. This is not due to the small number of lines that were used in the deconvolution or to blending. In fact, all the strong silicon lines were inspected individually and showed the same asymmetric shape. Catala et al. (1999) found very marked differences between different ionization species and elements for AB Aurigae, where an extra emission component was seen in the higher ionized species. Unfortunately, the singly ionized lines in SU Aur are too weak and too blended to carry out a similar analysis.

As far as the line variability and the line-profile deformations are concerned, it appears that there is no difference between the various subsets or indeed the LSD profiles obtained using all available lines, so that using all lines in the spectrum should be a valid approach. Unfortunately, the S/N level of the smaller subsets is too low to quantify the agreement (or indeed the disagreement) between them. We decided to err on the side of caution and exclude possible artefacts due to the lighter elements and used only neutral lines of the heavier atoms for the Doppler images presented below.[1]

While least-squares deconvolution is necessary here to achieve a high enough S/N, it introduces problems not usually encountered in multisite Doppler imaging. This is due to the very different spectral ranges and the different setups at the five sites. This is shown in the middle graph of Fig. 14, where the mean profiles of all five sites are plotted. It turns out that the mean profiles at the INT and CFHT agree reasonably well, but that the profiles at BAO and MDO look very different. Given that not all phases are covered equally at the different sites, small differences in the mean profile can be expected. Nevertheless, the differences that we observe are too large to be attributed to a different phase coverage.

We suggest that the differences are mostly due to the different setups used at each observatory, for the following reasons. The number of lines registered for each spectrograph setup is different at each observatory. Therefore, even using the same starting list of lines can produce different mean profiles. This is because some lines are registered twice at some spectrographs or fall into gaps in the spectral coverage. The number of lines included in the LSD line list is given in the second column of Table 9 along with the actual number of line images (third column) and the 'central' wavelength of the deconvolved profile (fourth column). For the deconvolution, each line is weighted according to its line depth, giving least weight to the weakest lines. Furthermore, lines on the edge of the chip where the continuum flux level (and hence S/N) is low are also given reduced

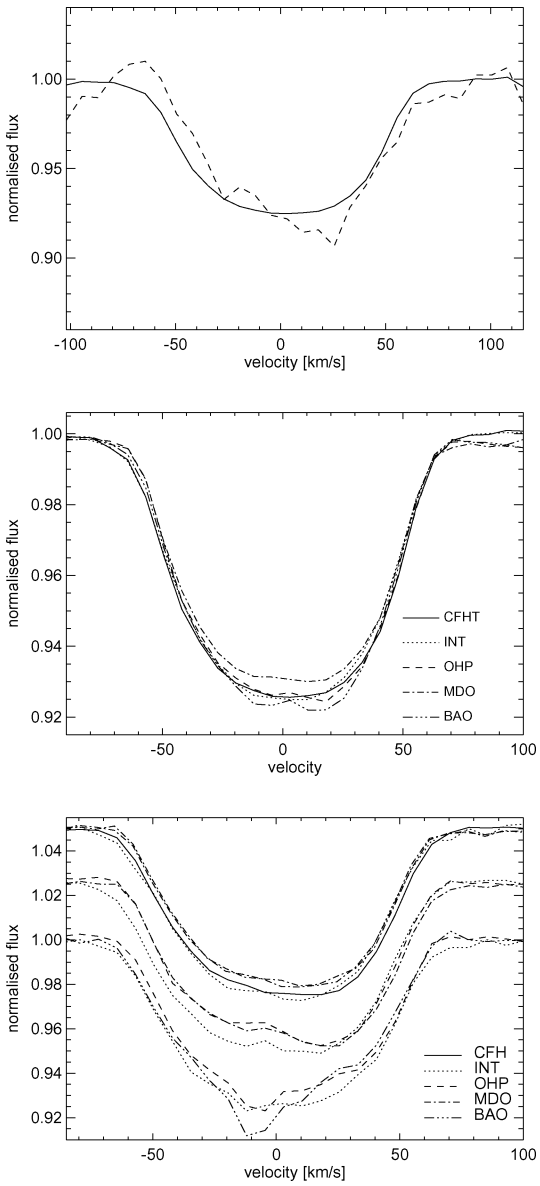

Figure 14. Top: Plots of different mean LSD profiles from the data taken at the CFHT. The solid line is the profile that has been obtained by deconvolving all neutral lines from elements heavier than (and including) calcium. The dashed line shows the mean profile of the four strongest unblended silicon lines. Middle: The rather different mean profiles at the five observatories. Bottom: Comparison of LSD profiles taken at approximately the same time but at different observatories. The profile deformations agree reasonably well between the different observatories, though there are some important discrepancies for some observations. The uppermost profiles were observed around modified HJD (MHJD = HJD – 245 0400) of 12.4. The thick and thin dot-dashed profiles show two profiles from the MDO taken about 3 h apart, corresponding to a phase difference of only 0.04. This phase difference is too small to show the motion of the surface features. The difference between the two profiles is probably due to noise. The middle profiles were observed between MHJD 8.7 and 8.8, and the bottom profiles between MHJD 7.7 and 7.9.

[1] We took care to exclude a large enough section around the rejected lines to avoid artefacts through blended lines.

Table 9. The number of lines used at the different observatories. The first column indicates the observatory. The second column gives the number of different lines used for the convolution. The third column lists the number of line 'images' that were actually used for the calculations. This number tends to be higher than the one given in column 2, as some lines were recorded twice on the chip. The last column gives the weighted central wavelength of the final profile. Note that we used the same line list for the CFHT and the INT.

Observatory	Lines	Images	λ_c (nm)
BAO	352	400	656.7
OHP	1828	2160	526.7
INT	950	1290	584.8
MDO	311	433	601.4
CFHT	1728	2660	563.3

weight. This latter weighting differs for each observatory. We tested the influence of this weighting for data from the CFHT and the INT. As the overlap between the spectral ranges at these telescopes is very high, we could use the same line list to produce two different mean profiles at each observatory, one of which takes S/N into account. The mean profiles at the INT and CFHT that neglect the error weighting are indeed very similar, so that the same template lookup table (see also Section 4.3) can be used for the INT and CFHT profiles.

More worrying than the small shape differences in the mean profiles of the different observatories are occasional differences in profile deformations observed at roughly the same phase that cannot be attributed to noisy data. This is illustrated in the bottom plot of Fig. 14, where profiles that were taken almost simultaneously at different sites are compared.[2]

4.2 Photospheric line-profile variations

We find marked shape changes in the photospheric line profiles as mirrored in the convolved profiles. This is shown in the grey-scale plot of the residual deconvolved line profiles in Fig. 15. The residuals have been produced by subtracting the mean profile of each observatory from the individual exposures at this observatory. Fig. 15 illustrates the major problem for Doppler imaging SU Aur. Despite the clear periodicities found in the He I D_3 and the Na D lines, no obvious periodicity appears to be present in the deconvolved photospheric lines. In fact, a periodogram analysis of the (mean-subtracted) deconvolved profiles does not show any significant peaks on the stellar rotation time-scale. We do not think that this is due to the differences in the mean profiles at the different observatories, as a periodogram analysis of the CFHT and INT profiles that were produced with identical weighting and that agree generally well also did not show any periodicities. This begs the question of whether large contrasting surface features are present on SU Aur or whether the line-profile changes are primarily due to causes other than starspots.

One such cause could be the strong dimming (usually attributed to circumstellar dust obscuration) that we observed around HJD 245 0410 (see Fig. 2). The time of the faintest observation coincides

[2] Note that the agreement between individual strong lines, such as e.g. Hα, that were observed at different observatories but at similar times is very good. This suggests that the discrepancy arises mainly because of the low S/N.

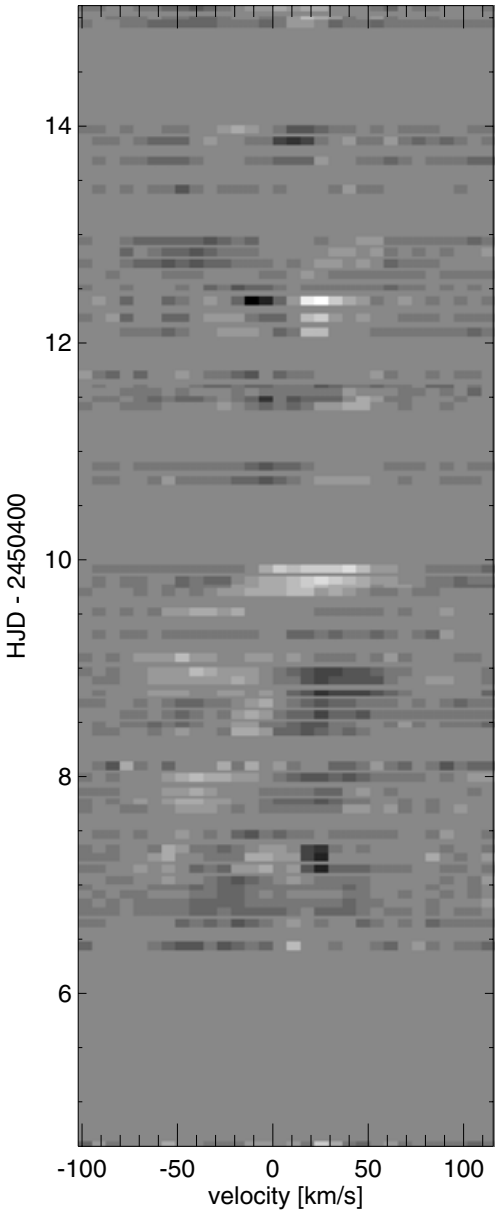

Figure 15. A stacked plot of the residuals of the deconvolved profiles. White is at a flux level of 1.008 and black at a flux level of 0.992.

reasonably well with one of the peaks in the He equivalent width and it is preceded by a very strong flux increase in the Hα line. The behaviour of the LSD profiles during the dimming is somewhat ambiguous, though the observations at the MDO that cover this time-span best suggest a decrease of the equivalent width from 5 per cent above average at HJD 245 0409 (Hα maximum) to 5 per cent below average at HJD 245 0410 (He maximum). Note that the scatter of the LSD equivalent widths is of the order of 3 per cent at the MDO. If the variations in the light level were veiling-like, e.g. if they arose from excess emission due to hotspots, low light levels should entail increased photospheric linewidths, which does not fit in well with our observations.

The predictions for the He line depend on what line formation scenario is assumed. If the He absorption is produced in the hotspot, the He equivalent width should be at a maximum during large veiling, though there might also be a dilution effect due to the excess

emission. If, however, the spot produces He emission and line infilling, we would expect the He equivalent width to anticorrelate with the broad-band emission. While we lack high-time-resolution photospheric observations, a comparison between the light curve of SU Aur and the variations in the He 587.6 nm line does suggest that their variability time-scales are different and that their variability is not correlated. This favours a scenario where the periodic He equivalent width variations are produced in dense infall columns or hotspots whereas the more erratic photometric variability is mainly due to dust. It is likely that the photospheric equivalent widths are due to a combination of both effects, thus masking any clear trends and periodicities.

We checked for indications of a colour change as a consequence of the photometric dimming. For the INT, which offers a relatively good time and wavelength coverage, there is no discernible trend distinguishing the lines redward and blueward of 650 nm. The high-S/N data of the CFHT also did not show any colour trend. This is in good agreement with the findings by Herbst & Shevchenko (1999). While we do not see any colour changes during the dimming event, we do find that, as SU Aur became fainter, i.e. from around HJD 245 0408.0 onwards, all profiles show a strong asymmetry, with the flux in the red part of the profile being suppressed. It appears that this effect is strongest for the singly ionized lines while hardly visible for neutral lines with low atomic numbers (such as sodium, magnesium and silicon). The profiles remain very similar for at least 1.2 d (see Fig. 15). As it takes roughly one-third of a rotation period for a spot to cross the visible hemisphere of the star, this line asymmetry is clearly too long-lived and too stationary to be produced by a surface spot. Whether the asymmetry and the dimming are really linked is difficult to establish as the photometric observations are only very sparsely sampled.

Whatever the cause of the profile asymmetry, reconstructions based on the complete data set will run into difficulties. We therefore reconstructed images where the profiles between HJD 245 0407.75 and 245 0409.0 have been excluded (see next section). Even then we struggle with an apparent lack of periodicity. This is visible in the phase-binned residuals shown in Fig. 16, where some of the neighbouring spectra show very different features. Any selected trial period between 2.3 and 3.3 d produced similarly disjoint plots, suggesting that the surface of SU Aur changes on the time-scale of one stellar rotation. It is likely that we see a mixture of line-profile deformations that are due to spots, to non-surface events and to dynamic short-lived events.

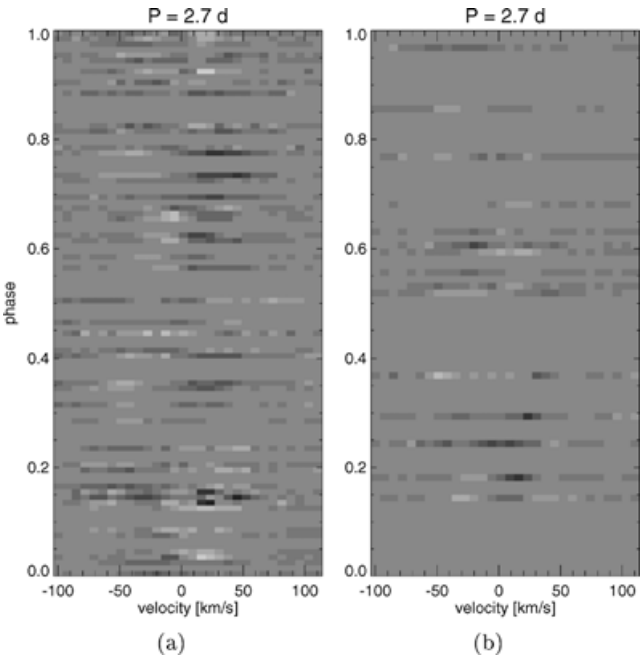

Figure 16. (a) The residuals as in the previous figure, but binned according to a period of 2.7 d. (b) A similar figure, except that only the profiles from the CFHT and INT have been included. We have also excluded the first profile at the INT (taken at HJD 245 0404.6, well before the remainder of the data) and the profiles during the 'dimming'. The grey-scale runs from a flux level of 0.992 (black) to 1.008 (white) for (a) and from 0.995 to 1.005 for (b). It is evident that some profiles do not fit in well with adjacent profiles. This is in part due to noise (see also the previous figure), but also due to a lack of repeated structure and the insecurity in the stellar period.

4.3 Doppler images

Despite all these problems, we tried to construct several Doppler images over different time-spans in the hope of recovering identical features that would allow us to exclude shorter-lived disturbances. We chose an ephemeris of HJD 245 0409.6. This was picked arbitrarily to correspond to the mid-data set maximum He I absorption. So as to be able to differentiate between more persistent structures and very short-lived features as well as possible artefacts, we ran test reconstructions of data subsets where we excluded certain days or also data from individual observatories.

The reconstruction parameter of the code that we employ for the Doppler imaging is the spot filling factor: each pixel on the stellar surface is characterized by the amount that it is covered in spots (see e.g. Collier Cameron & Unruh 1994; Barnes et al. 1998). We assumed the photospheric temperature to be 5500 K and used the LSD profile of the Sun as a lookup table for the immaculate photosphere.[3] This profile is in principle different for each observatory, though it turned out that we could use the same template profile at the INT and CFHT, provided the lines were only weighted by their depths. Whether a depth-only weighting is chosen or whether the flux level is also taken into account at the CFHT and INT does not have a noticeable effect on the resulting images and fits.

It is not entirely clear what temperature and line profile to adopt for the inhomogeneities. On the one hand, the relatively constant equivalent width suggests that any excess flux, e.g. due to hotspots, is not strongly modulated. The erratic changes in the line profile, on the other hand, are untypical for cool spots, at least in the framework of other active-star observations. We tried three different assumptions for the inhomogeneities: one where the profile changes are due to cool spots; one where they are due to hotspots with a 'stellar' atmospheric structure; and one where the hotspots only emit a continuum blackbody spectrum, i.e. where no absorption line is observed for the hot structures.

Depending on which phases and observatories were included in our reconstructions, periods ranging from 2.5 to 3.1 d yielded the best fits with Doppler images that did not show obvious artefacts or very fragmented spot coverage. For the images presented here, we chose a period of 2.7 d, as this agrees best with the periods deduced from the analysis of the Hβ, Na D and He I lines. We further assumed

[3] We found that using a different template star (e.g. the slightly cooler HD 217014) does not change the fits, as the equivalent width of the profile is adjusted to match the equivalent width of SU Aur at each observatory. These adjustments are usually very small; large offsets would indicate that the template is not suitable.

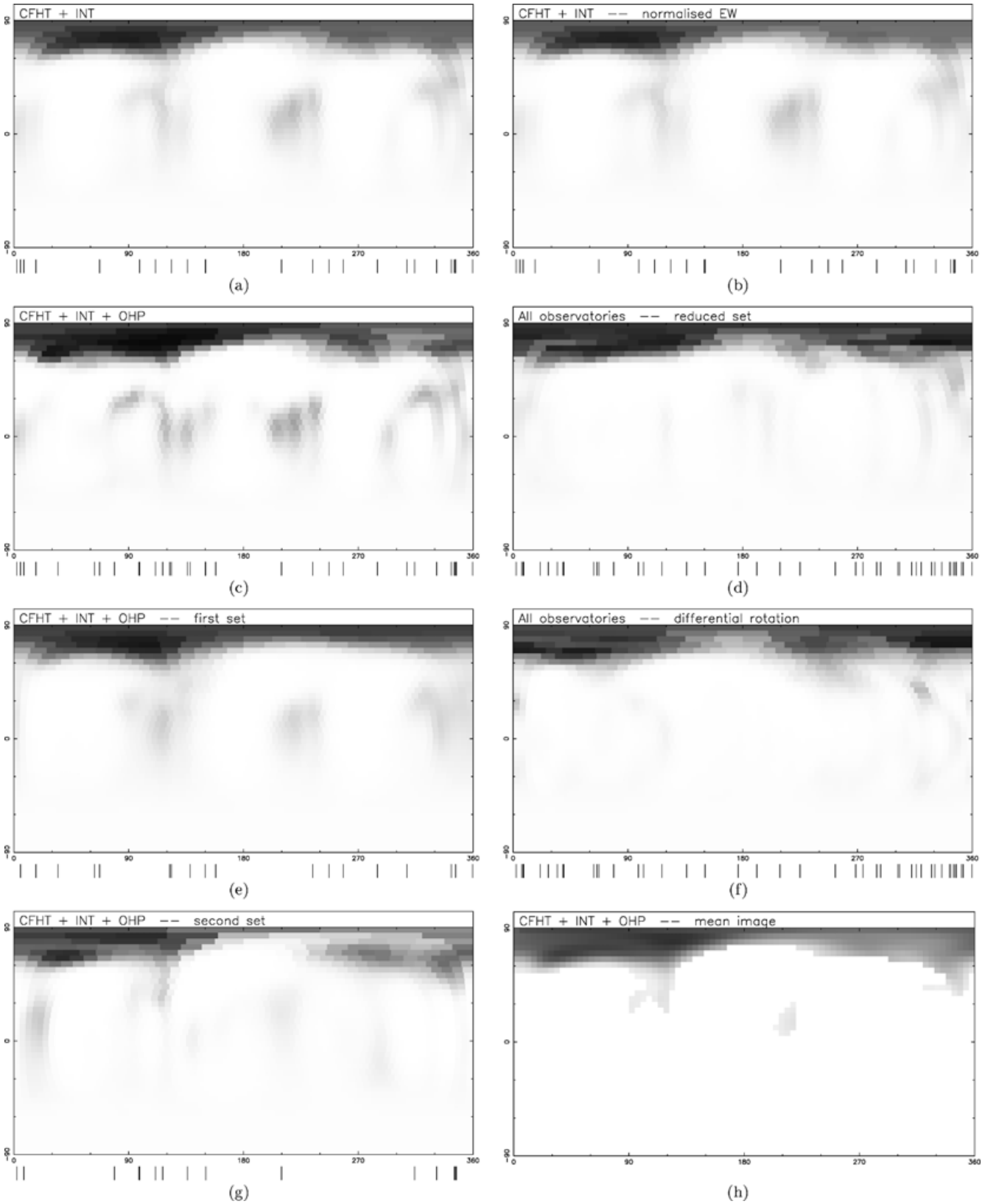

Figure 17. Doppler images. The reconstruction parameters and the data sets used for the different images are listed in Table 10, along with the spot filling factors and the goodness of fit. The lines underneath the images indicate the phases at which the data used for the reconstructions were taken.

Table 10. List of parameters used for the reconstructions of the Doppler images shown in Fig. 17. The first column lists the identifier. Columns 2 to 4 list the goodness of fit for different data subsets: $\chi^2_{\rm f}$ gives the goodness of fit for the actual fit (using the data as listed); $\chi^2_{\rm t}$ lists the goodness of fit between the complete data set and the predicted profiles; and χ^2_{-} lists the goodness of fit between the predicted profiles and a data set that excludes profiles from BAO and profiles taken between HJD 245 0407.75 and 245 0409.0 (see also dashed lines in Fig. 18). Column 5 shows the spot filling factor. Columns 6 to 10 indicate which time-spans of the data have been used in the fits for each observatory. The times are listed in modified HJD (MHJD), i.e. HJD – 245 0400; a dash indicates that no data from the particular observatory were used; and 'excl' indicates that all profiles were used for a given observatory except for profiles taken between MHJD 7.75 and 9.0. Row (h) is the (thresholded) mean image obtained from rows (e) and (g); and row (19) refers to the hot-spot image shown in Fig. 19. The last two rows list $\chi^2_{\rm t}$ and χ^2_{-} for unspotted input images, including and excluding differential rotation.

Image	$\chi^2_{\rm f}$	$\chi^2_{\rm t}$	χ^2_{-}	$A_{\rm s}/A_*$ (per cent)	BAO	OHP	INT	MDO	CFHT	Comments
(1)	(2)	(3)	(4)	(5)	(6)	(7)	(8)	(9)	(10)	(11)
(a)	1.2	2.2	1.7	5.1	–	all	all	–	–	
(b)	1.1	2.2	1.6	4.8	–	all	all	–	–	normalized EW
(c)	1.2	2.0	1.5	6.5	–	all	all	–	all	
(d)	1.2	1.9	1.2	5.1	excl	excl	excl	excl	excl	
(e)	1.3	2.3	1.8	5.2	–	6.4–8.7	7.5–9.7	–	6.9–9.1	
(f)	1.2	2.1	1.2	4.8	excl	excl	excl	excl	excl	diff. rot., $D_{\rm r} = -0.1$
(g)	1.0	2.4	1.7	4.4	–	11.4–12.4	11.5–13.4	–	13.9–15.1	
(h)	–	2.2	1.6	2.8	–	–	–	–	–	
(19)	1.0	1.8	1.4	3.3	–	all	all	–	–	
blank	–	4.1	3.3	0.0	–	–	–	–	–	
blank	–	4.0	3.0	0.0	–	–	–	–	–	diff. rot., $D_{\rm r} = -0.1$

the inclination angle to be 60°. The inclination angle can usually be estimated by determining the best possible fits as a function of the inclination angle. In our case, where the stellar period is not known exactly, we determined the best-fitting inclination angle for a range of periods. The angles were only weakly dependent on the period and we settled on 60°, as this yielded good fits for periods around 2.7 d. It is also in good agreement with the analysis of infrared and millimetre observations by Akeson et al. (2002), who found an inclination angle of 62^{+4}_{-8} deg. For our values of the period, rotational velocity and inclination, we calculate a stellar radius of approximately 3.6 solar radii (see also Section 6).

4.3.1 Cool spots

For the cool-spot solutions shown in Fig. 17, we assume a spot temperature of 4500 K. The top row shows two images produced from data at the CFHT and INT. For the image on the right-hand side, the profiles were rescaled to the mean equivalent width. Both images are very similar, though the rescaled images require a smaller surface coverage to achieve an equally good fit. Figs 17(c), (e) and (g) show images obtained from observations at the CFHT, INT and OHP. While image (c) is for all available data spanning more than three rotation periods, images (e) and (g) are for roughly one rotation period centred on HJD 245 0407.8 and 245 0413.2 respectively. The contributing observatories and the selected time-spans for all the images are listed in Table 10. Also listed are the values for χ^2 for the actual fit, the total data set and a reduced data set where the dimming event and the profiles from the BAO that show the lowest S/N have been excluded. The fits that result in Fig. 17(d) are shown in Fig. 18. The solid lines are the fits and the dashed lines are the predicted spectra for the phases that were not considered in the fits (due to the dimming event).

In order to improve the fits to the line profiles, we have included differential rotation into our Doppler imaging code, according to $\Omega(\theta)/\Omega_{\rm eq} = 1 - D_{\rm r} \sin^2(\theta)$. In agreement with Johns-Krull (1996) we find that differential rotation coefficients of about $D_{\rm r} = -0.1$ yield marginally better fits with smaller spot coverage (compare rows 'd' and 'f' in Table 10). Changes in the differential rotation coefficient require adjustments in the value for $v \sin i$. For a differential rotation coefficient of -0.1, we obtain the best fits for $v \sin i = 58$ km s^{-1}, while $v \sin i = 59$ km s^{-1} yields the best fits if no differential rotation is assumed. For solid-body rotation, the spot coverage is higher at intermediate to high latitudes than for differential rotation. The location of the surface features, however, remains the same irrespective of whether differential rotation is included or not. This is illustrated in Figs 17(d) and (f). Image (f) is for a differential rotation coefficient of -0.1, whereas image (d) has no differential rotation.

4.3.2 Hotspots

The magnetospheric disc accretion model predicts hotspots or bands at high stellar latitudes. If such hotspots are unevenly distributed and are much hotter than the photosphere, or cover a large fraction of the surface, their excess emission should produce a variable dilution of the photospheric line profiles (veiling) in addition to lineshape changes. We do not see any consistent trend above the 2.5 per cent scatter in the equivalent widths of the LSD profiles, and previous optical veiling determinations have yielded null results for SU Aur [see Basri & Batalha (1990) and Johns & Basri (1995b), though note also that Folha & Emerson (1999) found SU Aur to be highly veiled in the infrared *K* and *J* bands].

In a first attempt, we assumed that the spot spectrum would be represented by an ordinary hot-star spectrum. It turned out, however, that no satisfactory fits could be obtained if the convolved hotspot spectrum showed a significant absorption line. This led us to try fits where the spot produces a pure blackbody spectrum. Temperatures of 6000 and 6500 K yielded slightly better fits than the cool-spot assumption while needing only very small spot-covering fractions of around 3 per cent. Fig. 19 shows an example image obtained using data from the CFHT and INT. Note that the location of the spot features essentially agrees with that found from the cool-spot

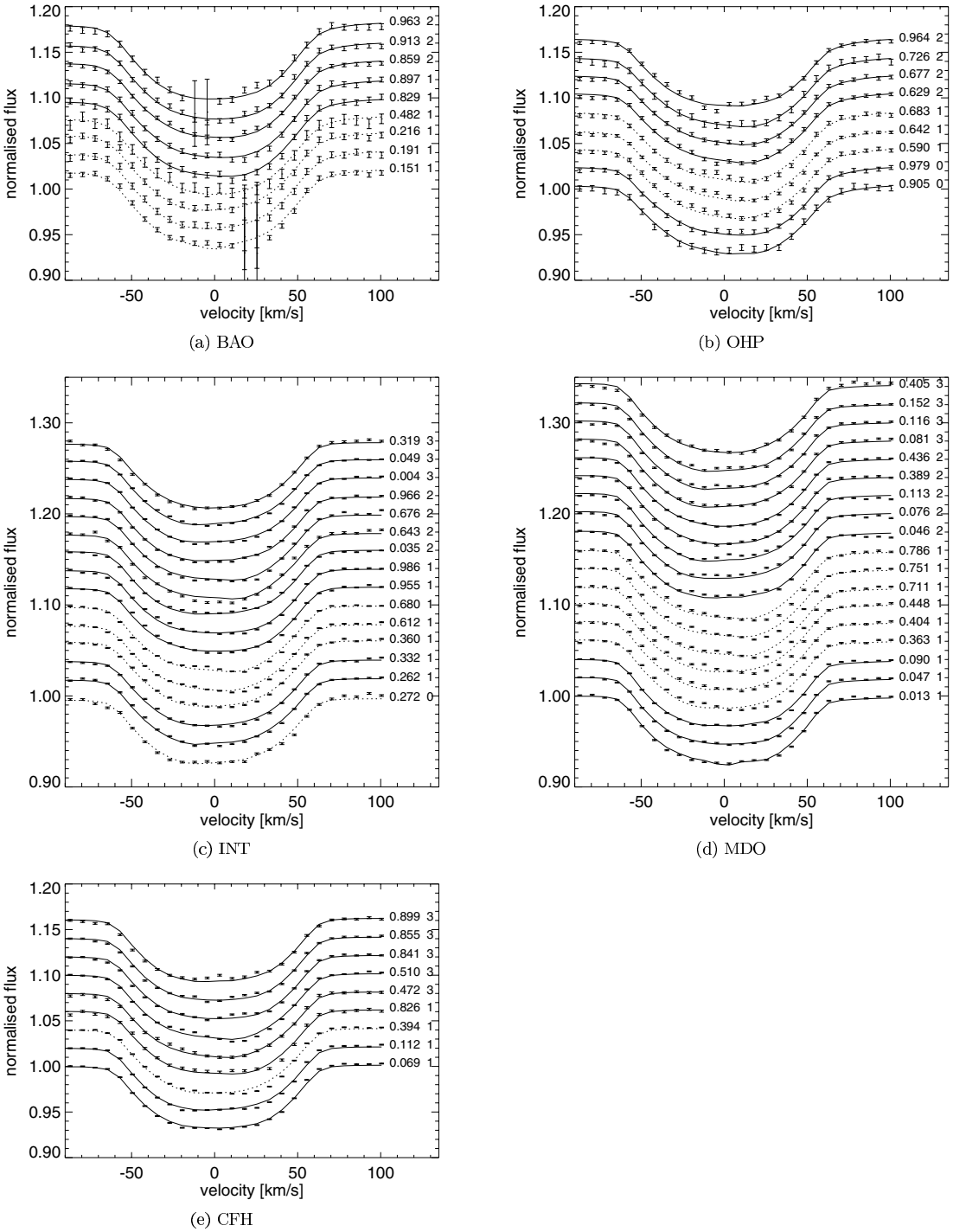

Figure 18. The LSD profiles along with the fits (solid lines) and the predicted theoretical profiles (dashed lines) for the different observatories. The data are shown as dots along with their error bars. Only the data points overlaid with solid lines were used to obtain the Doppler image (shown in Fig. 17d). The dashed lines are the predicted profiles from Fig. 17(d) for those phases that were excluded from the fit as they might be affected by a dimming event not related to a change in the surface structure. At the INT, we also excluded the very first exposure as it was taken almost a whole rotation period before the next set of observations. The numbers labelling the profiles are the phase of the profile (assuming a 2.7-d period and an ephemeris of HJD 245 0409.6) and a rotation count number. The observatories where the data were taken are indicated below each panel.

fits (Figs 17a and b) to the same data set. This is not surprising, as it is the decreasing total flux for the cool spot rather than the shape of the cool-spot spectrum that acts as the main factor in producing the line-profile deformation. Our method does not allow us to determine an accurate hotspot temperature, as the size of the deformation is a function of the temperature and the surface coverage. We find, however, that the goodness of fit starts to deteriorate and the reconstructed images start to show strongly fragmented spots for temperatures above 7000 K. For very high temperatures, the veiling predicted by the spots that are invoked to fit the line-profile

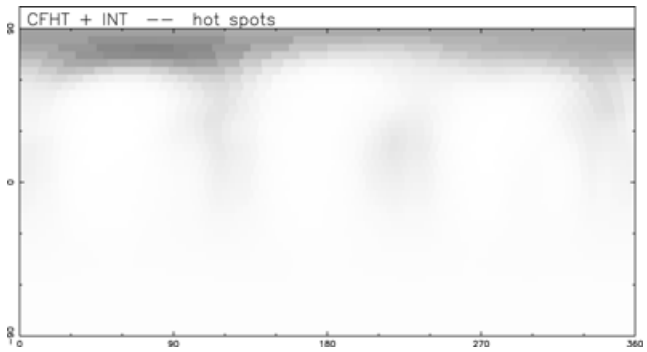

Figure 19. Doppler image for continuum hot (6000 K) spots. Note that, as on previous plots, the photosphere is left white, while grey indicates the spot filling factor. The total surface covered by the hotspots here is 3.3 per cent.

deformations is no longer compatible with the relative constancy of the line equivalent width.

4.3.3 Comparison between different Doppler images

Whilst the agreement between the different Doppler images is not very convincing at first sight, there are features that can be found on almost all of the images. To highlight those features, we created a 'thresholded mean image' of the Doppler images displayed in Figs 17(e) and (g). To create this image, we only attributed spots to those pixels where the spot-filling factor in both contributing images was above a certain threshold, in this case greater than 5 per cent. The features visible on the 'thresholded mean image' (see Fig. 17h) are hence features that were present on both input images. As image (e) is based on data taken between MHJD 6.4 and 9.7, whereas image (g) is based on data taken between MHJD 11.4 and 15.1, the mean image should show the pixels where structure was present (and possibly survived) after more than one stellar rotation had passed.

The mean image in Fig. 17(h) shows mainly high-latitude features. In fact, most images, including Fig. 19 for the hotspots, recover two high-latitude spotted areas (between longitudes 30° and 112° and from about 270° to 350°) that are made up of a couple of stronger spots. Also shown on most images are some low- and intermediate-latitude spots around approximately 120° and 210° longitude. Note that the thresholding biases against low-latitude structure. This is because the longitude resolution is latitude-dependent and much higher at low latitudes. Errors in the period and differences in the phase coverage produce small longitude shifts. These are particularly noticeable for narrow elongated low-latitude features. The shifts then result in structure being suppressed on the thresholded image.

While we cannot exclude the presence of hotspots with stellar-like atmospheres, the fits for cool spots or for blackbody hotspots yield much better goodness-of-fit parameters and less fragmented surface images. While we cannot decide on the basis of our data whether the spots are hot or cold, or whether there is indeed a mixture, the lack of repeatability in the photospheric line profiles does favour the hotspot scenario. The lowest high-latitude spot covering fractions are seen around longitudes 180° to 210°, i.e. roughly out of phase with the maximum He D_3 equivalent width, and would fit in very well with the 'eggbeater' scenario.

It is heartening that the mean image is very similar to the image reconstructed from all the data except those profiles that might be contaminated by the 'dimming event' (Fig. 17d). This event is mostly visible for the data at the MDO, for which the discrepancy between the predicted line profiles and the actual line profiles as shown in Fig. 18 is largest. The goodness-of-fit values for the mean image are listed in row (h) of Table 10. Note that the light curve of SU Aur shows very erratic behaviour. This may mean that the stellar surface as we observed it during the MUSICOS campaign was not 'typical', if there is indeed a 'typical' spot coverage for SU Aur. We therefore do not expect our images to show much similarity with previous or future images.

5 MAGNETIC FIELD MEASUREMENTS

The exposures (nine groups of four subexposures) obtained at the CFHT with the MUSICOS spectropolarimeter can be used to extract information about the magnetic field structure of SU Aur. The first step in this process consists of extracting the LSD Stokes *V* signatures from all available photospheric lines. To maximize our chances of detecting the field, we convolved all spectral lines whose relative depth (prior to any kind of macroscopic broadening) exceeds 10 per cent of the continuum level in an ATLAS9 G2 subgiant synthetic spectrum (Kurucz 1993). As a result, about 3500 lines were used in the analysis. We averaged all spectra obtained on the same nights whose rotational phases are within a few per cent of each other, thereby decreasing the noise level in the resulting circular polarization profiles further. From the original nine profiles we thus obtain five LSD Stokes *V* spectra that correspond to rotational phases of 0.09, 0.39, 0.83, 0.49 and 0.87, with relative noise levels of 0.031, 0.040, 0.100, 0.042 and 0.037 per cent respectively. The strongest signature we see is observed at phase 0.09 on 1996 November 19 (see Fig. 20). With a peak-to-peak amplitude of 0.15 per cent (5σ), this signature is associated with a detection probability of only 94 per cent. We therefore consider that this detection is only very marginal, confirming that SU Aur is an interesting target for future magnetic field investigations with more sensitive spectropolarimeters.

One can note that the shape of the marginal Zeeman signature discussed above, if real, is rather complex, with at least three polarization sign switches throughout the line profile. This suggests that the associated surface field topology is not simple. It is reminiscent of the polarization signatures detected on the weak-line T Tauri stars V410 Tau and HDE 283572 with a similar instrument (Donati

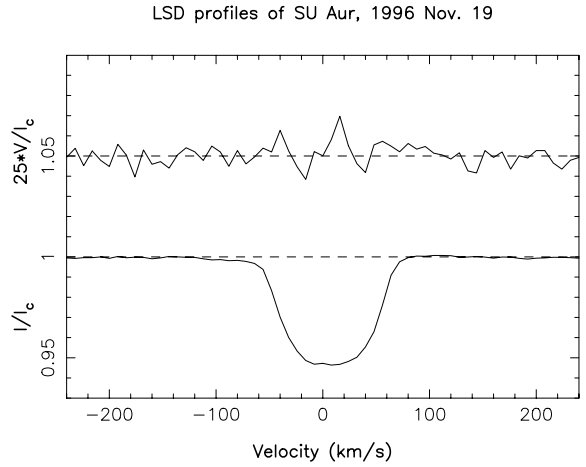

Figure 20. The Stokes *I* (bottom) and *V* (top) least-squares deconvolved profiles of SU Aur on 1996 November 19. Both profiles have been normalized. The Stokes *V* profile has been shifted by 0.05 and amplified by a factor of 25 so as to show the structure in the line more clearly.

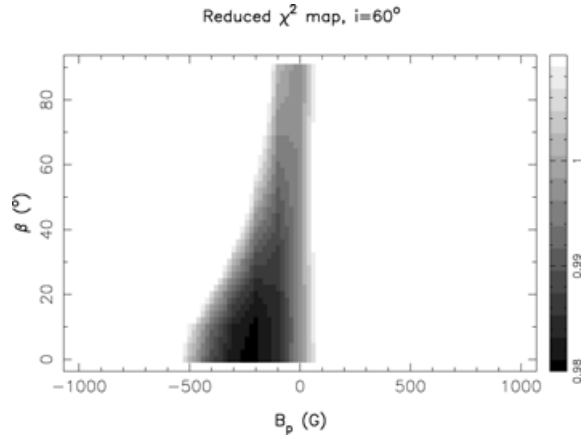

Figure 21. Contours of reduced χ^2 between synthetic and observed Stokes *V* profiles. The *y*-axis shows the inclination of the magnetic axis to the rotation axis, while the *x*-axis shows the strength of the dipole field. The two darkest grey levels correspond to models within the 68 per cent confidence limit, while white corresponds to models outside the 99 per cent confidence limit. Field strengths that yield acceptable fits for an inclined magnetic axis are rather small, ranging between about −300 and 100 G.

et al. 1997), that also argue in favour of a rather complex field structure such as that reconstructed on the older zero-age main-sequence (ZAMS) star AB Dor (Donati & Cameron 1997). We nevertheless investigated the suggestion of Johns & Basri (1995b) that the magnetic field of SU Aur is largely dipolar, with the magnetic axis inclined with respect to the rotation axis. In this model accretion occurs mainly at the magnetic poles. Although this assumption may sound rather incompatible with the above conclusions that the field is complex, it can none the less be useful to estimate the upper limit to the dipole field strength that our data can allow.

We therefore computed a number of synthetic Stokes *V* spectra for various dipole models, which we compare with our nine LSD Stokes *V* profiles with the help of a simple χ^2 statistic.[4] While the phase at which the magnetic pole comes closest to the line of sight is fixed to that at which the He I line at 587.6 nm exhibits its strongest absorption (i.e. at phase 0.0 in the ephemeris mentioned above), the strength of the dipole field and the inclination of its axis with respect to the rotation axis are considered as free parameters, in the range of −1 to 1 kG and 0° to 90° respectively. For all these models, we compute the reduced χ^2 test between the synthetic and observed Stokes *V* profiles, and display it as a map in Fig. 21. We can thus conclude that the strength of such a dipole field must range between −500 and 100 G to remain compatible with our observations (at a 68 per cent confidence level). Moreover, given the fact that the range of reasonable orientations of the magnetic axis with respect to the rotation axis is rather 30° to 60° (to ensure that one pole is much more visible than the other and that accretion is only observed during one half rotation cycle), we finally obtain that the maximum dipole field strength ranges between about −300 and 100 G.

It is difficult to see how such a weak field will be able to magnetically confine material accreted at a rate of 6×10^{-8} $M_\odot$ yr^{-1} at a distance of about two stellar radii (where the local field strength is weaker than 20 G). This suggests that, while the eggbeater model successfully explains many of the basic phenomena observed on SU Aur and how material is accreted on to its surface, the details of the magnetic interaction between the central star and circumstellar disc are likely to be more complex. We checked for circular polarization signatures in the He I line at 587.6 nm such as those reported by Johns-Krull et al. (1999a) on the classical T Tauri star BP Tau. No features above the noise level are seen in the vicinity of the He I line.

[4] The results described hold also for the co-added set of five LSD profiles.

6 DISCUSSION AND CONCLUSIONS

6.1 Stellar parameters

Our analysis confirmed a projected rotational velocity of approximately 60 km s^{-1} for SU Aur, while the rotation periods determined from different lines are all below the previously determined rotation period of 3 d. Together with our estimate of the inclination angle obtained from the Doppler imaging procedure, this allows us to re-evaluate the stellar parameters. Unfortunately, the errors on our period determinations and also on the inclination angle are fairly large, so that we can only give a somewhat large range of probable radii.

For a rotation period of 2.7 d, we find that the Doppler imaging process favours inclinations between 50° and 70°. The projected rotational velocity of 59 ± 1 km s^{-1} hence translates into an equatorial rotation velocity $v_{\rm eq} = 68^{+10}_{-6}$ km s^{-1}. Using $R = Pv_{\rm eq}/2\pi$, we obtain a stellar radius of $3.6^{+0.6}_{-0.3}$ $R_\odot$. The smallest radius possible for a period of 2.7 d is 3.0 $R_\odot$. The uncertainty on the stellar period is quite large, and periods of 2.5 and 2.9 d, which are also plausible, would yield smallest radii of 2.8 and 3.3 $R_\odot$ respectively.

Akeson et al. (2002) found that an inner radius of 0.05 to 0.08 au for the *K*-band emission yielded the best model fits. This would correspond to about 2.7–4.3 stellar radii. This is in very good agreement with the usual assumption of the magnetospheric accretion model that the inner disc starts at the corotation radius. Depending on the exact parameters adopted for the stellar mass, radius and rotation period, the corotation radius of SU Aur is at about 2.5–3 stellar radii. Any of the inner disc edges cited above are large enough to prevent occultation of the star by the disc. Indeed, for a system seen at an inclination of 60°, the disc would have to start at 0.7 stellar radii from the surface in order to occult the star.

The derived radii tie in well with the *Hipparcos* parallax and the colour of SU Aur. The *Hipparcos* catalogue (ESA 1997) lists a parallax of $(6.58 \pm 1.92) \times 10^{-3}$ arcsec, a colour of $B - V = 0.833$ mag and a *V*-band brightness of 9.23 ± 0.056 mag. The absolute (non-extinction-corrected) *V*-band magnitude of SU Aur is hence $3.3^{+0.6}_{-0.8}$ mag. The bolometric correction is independent of the stellar luminosity class and is −0.2 mag for the colour term given above (Lang 1980). The interstellar extinction has been given as $A_V = 0.9$ mag by Chen et al. (1995) and as $A_V = 0.93 \pm 0.14$ mag by Cohen & Kuhi (1979), while the prescription given in Hillenbrand (1997) yields $A_V = 0.46 \pm 0.23$ mag. Using an extinction of 0.9 mag, we obtain a corrected bolometric absolute magnitude of $2.2^{+0.6}_{-0.8}$. For a blackbody, $M_{\rm bol}$ (in magnitudes) is related to its radius (in $R_\odot$) and temperature (see Lang 1980) through

$$M_{\rm bol} = 42.31 - 5 \log R - 10 \log T. \quad (1)$$

Using a temperature of 5700 ± 100 K, we obtain a radius of $3.2^{+1.4}_{-0.5}$ $R_\odot$. Note that these radii (along with the colour of the star) suggest that SU Aur is a subgiant rather than a giant.

The bolometric magnitude of SU Aur translates into a luminosity of $10.2^{+9.2}_{-2.5}$ $L_\odot$. According to the evolutionary tracks by D'Antona & Mazzitelli (1994) (using the convection description by Canuto & Mazzitelli 1992), the mass of SU Aur has to lie between about 2 and 2.5 $M_\odot$, while its age is around 3×10^6 yr. This is in reasonable

agreement with the findings of Dewarf et al. (1998), who determined a mass of 1.9 ± 0.1 $M_\odot$ and an age of 4×10^6 yr. The large age difference is mainly due to the different extinction corrections that were applied.

6.2 Variability

SU Aur is certainly a very complex system. While it displays some clear periodic features, notably in the Balmer lines, we also found short-lived and non-periodic features that make the interpretation of the system rather difficult. We find that the model by Johns & Basri (1995b) is on the whole successful in explaining the variability of the Balmer lines, Na D and He D_3, as well as the correlations between those lines. A more in-depth analysis of time-lags and cross-correlations between the different lines was presented in Oliveira et al. (2000), where some problems of the model along with possible extensions were also described.

During the MUSICOS 1996 campaign, we observed transient features in the blue wings of the Hα, Hβ and Na D lines. While they appear roughly contemporaneous in all lines, their velocity shifts and strengths differ from line to line. Whether the two events are due to the same mechanism is not clear, as they show different strengths and time behaviour (see also Oliveira et al. 2000).

From the analysis of the Balmer lines, He I (543.6 nm) and Na D, we find strong indications for a stellar rotation of the order of 2.8 d, albeit with relatively large uncertainties, mainly due to the non-sinusoidal nature of the variations combined with the relatively short observation time-span. The picture is less clear for the photospheric lines. The LSD profiles do not show any clear periodicities, and leaving the period variable in the Doppler image reconstructions yields different optimum periods (spanning 2.4 to 3.2 d) for different data subsets.

During the campaign, the *V*-band brightness of SU Aur dropped by 0.5 mag. This dimming seems to be coupled with a change in the line-profile shape of the photospheric lines. The convolved profiles show a redshifted emission feature for a duration of about 1.2 d, almost half a stellar rotation period. The most common explanation for the rapid dimmings of ETTS is that circumstellar matter obscures the stellar disc. This is not normally expected to influence the shapes of the photospheric line profiles. We suspect that not the complete stellar disc is obscured. There does not seem to be a change in the equivalent widths of the photospheric lines due to the dimming. The fact that we could also not find a wavelength-dependent behaviour of the equivalent width suggests that the obscuring matter is grey.

The dimming is also associated with an increase in the equivalent width of the (blue) Hα emission wings, and increases in the blue emission peak and the red wing for velocities below about 150 km s^{-1} (see also Fig. 5). If the equivalent width of the emission peak is plotted against magnitude, we find that there is a clear trend of decreasing equivalent width with increasing brightness. While the *V*-band brightness drops by 0.5 mag, the equivalent width increases by more than a factor of 2. No such trend is observed for the blue emission peak of Hβ even though there is otherwise a good correlation between the blue wings of Hα and Hβ. The fact that no line other than Hα shows a correlation with the broad-band magnitudes suggests that we are not dealing with a contrast effect. We would like to note, however, that the S/N is poor in the Hβ and photospheric lines, so that available matches between well-determined equivalent widths and photometric measurements are few.

While the least-squares deconvolved profiles contain a certain amount of non-repeated and probably also spurious structure (see e.g. the line depression at about 25 km s^{-1} for several BAO profiles), the images reconstructed from various data sets all show some consistent high-latitude features as in Fig. 17(h). This is a strong indication that SU Aur is indeed covered by some surface spots that last at least a few stellar rotations.

We also want to caution that the surface spots pictured in Fig. 17(h) cannot be the only features producing line deformations. This is illustrated by the only moderate improvement of the 'goodness of fit' compared to what one gets from a non-spotted star (see Table 10). Note that even the stacked residual profiles (leaving apart any period problems) show very few events that look like surface spots (see Fig. 15). There are a couple of such events, e.g. between about HJD 245 0407 and 245 0408 and then shortly before 245 0410, but nothing obvious later than that. SU Aur very likely presents a mix of periodic (spot or accretion curtain induced) variability typical for late-type TTS and the more erratic light-level changes typical for ETTS (UXORs) that are probably due to variations in the circumstellar dust. Our data suggest that some of the ETTS (or type III, Herbst et al. 1994) variability also affects the shape of the photospheric line profiles.

ACKNOWLEDGMENTS

The work reported in this paper is based on observations obtained during the 1996 Multi-Site Continuous Spectroscopy (MUSICOS) campaign, collected at the Canada–France–Hawaii 3.6-m telescope, the McDonald 2.1-m telescope, the La Palma 2.5-m Isaac Newton Telescope, the Observatoire de Haute-Provence 1.9-m telescope and the Xinglong 2.2-m telescope. The photometric data were obtained at the University of Vienna's automatic photometric telescopes. We are grateful for the efforts of the staff at all the telescopes involved. The authors gratefully acknowledge use of the Simbad astronomical data base. Extensive use was made of software provided through Starlink. We would like to thank an anonymous referee for very helpful comments and suggestions.

APH acknowledges the support of NSF Grant 9615571 and JDL acknowledges support from the Natural Sciences and Engineering Research Council of Canada. JMO acknowledges the financial support of Fundação para a Cincia e a Tecnologia from Portugal (Praxis XXI Grant BD9577/96) and of the UK Particle Physics and Astronomy Research Council (PPARC).

REFERENCES

Akeson R. L., Ciardi D. R., van Belle G. T., Creech-Eakman M. J., 2002, ApJ, 556, 1124
Andretta V., Giampapa M. S., 1995, ApJ, 439, 405
Armitage P. J., Clarke C. J., 1996, MNRAS, 280, 458
Baranne A. et al., 1996, A&AS, 119, 373
Barnes J. R., Collier Cameron A., Unruh Y. C., Donati J.-F., Hussain G. A. J., 1998, MNRAS, 299, 904
Basri G., Batalha C., 1990, ApJ, 363, 654
Basri G., Marcy G. W., Valenti J. A., 1992, ApJ, 390, 622
Baudrand J., Böhm T., 1992, A&A, 259, 711
Beichman C. A., Myers P. C., Emerson J. P., Harris S., Mathieu R., Benson P. J., Jennings R. E., 1986, ApJ, 307, 337
Bouvier J., Cabrit S., Fernandez M., Martin E. L., Matthews J. M., 1993, A&AS, 101(3), 485
Bray R. J., 1964, Z. Astrophys., 60, 207
Calvet N., Hartmann L., 1992, ApJ, 386, 239
Cameron A. C., Campbell C. G., 1993, A&A, 274, 309
Canuto V. M., Mazzitelli I., 1992, ApJ, 389, 724
Catala C. et al., 1993, A&A, 275, 245
Catala C. et al., 1999, A&A, 345, 884

Chen H., Myers P. C., Ladd E. F., Wood D. O. S., 1995, ApJ, 445, 377
Cincotta P., Méndez M., Núñez J., 1995, ApJ, 449, 231
Cohen M., Kuhi L. V., 1979, ApJS, 41, 743
Cohen M., Emerson J. P., Beichman C. A., 1989, ApJ, 339, 455
Collier Cameron A., Unruh Y. C., 1994, MNRAS, 269, 814
D'Antona F., Mazzitelli I., 1994, ApJS, 90, 467
Dewarf L. E., Guinan E. F., Shaughnessy T. M., 1998, Inf. Bull. Var. Stars, 4551
Dhillon V. S., Privett G. J., 1997, Starlink User Note 167.5, Rutherford Appleton Laboratory
Donati J.-F., Collier Cameron A., 1997, MNRAS, 291, 1
Donati J.-F., Semel M., Carter B., Rees D. E., Collier Cameron A., 1997, MNRAS, 291, 658
Donati J.-F., Catala C., Wade G. A., Gallou G., Delaigue G., Rabou P., 1999, A&AS, 134, 149
Eaton N. L., Herbst W., 1995, AJ, 110, 2369
Edwards S., Hartigan P., Ghandour L., Andrulis C., 1994, AJ, 108, 1056
ESA, 1997, The Hipparcos and Tycho Catalogues. ESA SP-1200. ESA Publications Division, Noordwijk
Folha D. F. M., Emerson J. P., 1999, A&A, 352, 517
Giampapa M. S., Basri G. S., Johns C. M., Imhoff C. L., 1993, ApJS, 89, 321
Grady C. A. et al., 1996, A&AS, 120, 157
Grinin V. P., Tambovtseva L. V., 1995, A&A, 293, 396
Grinin V. P., The P. S., de Winter D., Giampapa M., Rostopchina A. N., Tambovtseva L. V., van den Ancker M. E., 1994, A&A, 292, 165
Guenther E., Emerson J. P., 1996, A&A, 309, 777
Guenther E. W., Lehmann H., Emerson J. P., Staude J., 1999, A&A, 341, 768
Hartmann L., Hewett R., Calvet N., 1994, ApJ, 426, 669
Hatzes A. P., 1994, ApJ, 451, 784
Herbig G. H., Bell K. R., 1988, Lick Obs. Bull., Catalog of Emission Line Stars of the Orion Population, 3. Lick Observatory, Santa Cruz
Herbst W., Shevchenko V. S., 1999, AJ, 118, 1043
Herbst W. et al., 1987, AJ, 94, 137
Herbst W., Herbst D. K., Grossman E. J., Weinstein D., 1994, AJ, 108, 1906
Hillenbrand L. A., 1997, AJ, 113, 1733
Horne J. H., Baliunas S. L., 1986, ApJ, 302, 757
Horne K. D., 1986, PASP, 98, 609
Johns C. M., Basri G., 1995a, AJ, 109, 2800
Johns C. M., Basri G., 1995b, ApJ, 449, 341
Johns-Krull C. M., 1996, A&A, 306, 803
Johns-Krull C. M., Valenti J. A., Hatzes A. P., Kanaan A., 1999a, ApJ, 510, L41
Johns-Krull C. M., Valenti J. A., Koresko C., 1999b, ApJ, 516, 900
Joncour I., 1992, J. Astron. Fr., 43, 31
Joncour I., Bertout C., Ménard F., 1994a, A&A, 285, L25
Joncour I., Bertout C., Bouvier J., 1994b, A&A, 291, L19
Kenyon S., Hartmann L., 1987, ApJ, 323, 714
Königl A., 1991, ApJ, 370, L39
Kurucz R. L., 1993, ATLAS9 CDROM. Smithsonian Astrophysical Observatory, Cambridge MA
Lang K. R., 1980, Astrophysical Formulae, 2nd edn.Springer, Berlin
McCarthy J. K., Sandiford B. A., Boyd D., Booth J., 1993, PASP, 105, 881
Mills D., 1994, Starlink User Note 167.5, Rutherford Appleton Laboratory
Montgomery M. H., O'Donoghue D., 1999, in Breger M., ed., Delta Scuti Star Newsletter, Issue 13, p. 28
Myers P. C., Fuller G. A., Mathieu R. D., Beichman C. A., Benson P. J., Schild R. E., Emerson J. P., 1987, ApJ, 319, 340
Nadalin I., Dewarf L. E., Guinan E. F., 2000, Inf. Bull. Var. Stars, 4987
Oliveira J. M., Foing B. H., van Loon J. T., Unruh Y. C., 2000a, A&A, 362, 615
Petrov P. P., Gullbring E., Ilyin I., Gahm G. F., Tuominen I., Hackman T., Loden K., 1996, A&A, 314, 821
Press W. H., Flannery B. P., Teukolsky S. A., Vetterling W. T., 1992, Numerical Recipes: The Art of Scientific Computing, 2nd edn. Cambridge Univ. Press, Cambridge
Rice J. B., Strassmeier K. G., 1996, A&A, 316, 164
Roberts D. H., Lehár J., Dreher J. W., 1987, AJ, 93, 968
Saar S. H., Huovelin J., Osten R. A., Shcherbakov A. G., 1997, A&A, 326, 741
Safier P. N., 1998, ApJ, 494, 336
Shu F., Najita J., Ostriker E., Wilkin F., Ruden S., Lizano S., 1994, ApJ, 429, 781
Smith K. W., Lewis G. F., Bonnell I. A., Bunclark P. S., Emerson J. P., 1999, MNRAS, 304, 367
Stassun K. G., Mathieu R. D., Mazeh T., Vrba F. J., 1999, AJ, 117, 2941
Stellingwerf R. F., 1978, ApJ, 224, 953
Strassmeier K. G., 1994, A&A, 281, 395
Strassmeier K. G., Rice J. B., 1998, A&A, 339, 497
Strassmeier K. G., Boyd L. J., Epand D. H., Granzer T., 1997, PASP, 109, 697
Strassmeier K. G., Serkowitsch E., Granzer T., 1999, A&AS, 140, 29
Švestka Z., 1972, ARA&A, 10, 1
Unruh Y. C., Collier Cameron A., Guenther E. W., 1998, MNRAS, 295, 781

This paper has been typeset from a TEX/LATEX file prepared by the author.